The sulfur budget and sulfur isotopic composition of Martian regolith breccia NWA 7533

Jean-Pierre LORAND [ID][1]*, Jabrane LABIDI[2,3,4], Claire ROLLION-BARD[4], Emilie THOMASSOT[5], Jeremy J. BELLUCCI[6], Martin WHITEHOUSE[7], Alexander NEMCHIN[6], Munir HUMAYUN[8], James FARQUHAR[3], Roger H. HEWINS [ID][9,10], Brigitte ZANDA[9], and Sylvain PONT[9]

[1]Laboratoire de Planétologie et Géodynamique à Nantes, CNRS, UMR 6112, Université de Nantes, 2 Rue de la Houssinère, BP 92208, 44322 Nantes Cédex 3, France
[2]Geophysical Laboratory, Carnegie Institution of Washington, Washington, District of Columbia 20015, USA
[3]Department of Geology, University of Maryland, College Park, Maryland 20740, USA
[4]Institut de physique du globe de Paris, CNRS, Université de Paris, F-75005Paris, France
[5]CRPG-CNRS, Nancy 54500, France
[6]Department of Applied Geology, Curtin University, Perth, Western Australia 6845, Australia
[7]Laboratory for Isotope Geology, Swedish Mus. of Nat History, Stockholm SE-104 05, Sweden
[8]Department of Earth, Ocean & Atmospheric Science and National High Magnetic Field Laboratory, Florida State University, Tallahassee, Florida 32310, USA
[9]Institut de Minéralogie, de Physique des Matériaux, et de Cosmochimie (IMPMC) - Sorbonne, Université- Muséum National d'Histoire Naturelle, UPMC Université Paris 06, UMR CNRS 7590, IRD, UMR 206, 61 rue Buffon, 75005 Paris, France
[10]Department of Earth & Planetary Sciences, Rutgers University, Piscataway, New Jersey 08854, USA
*Corresponding author. E-mail: jean-pierre.lorand@univ-nantes.fr

Abstract–The sulfur isotope budget of Martian regolith breccia (NWA 7533) has been addressed from conventional fluorination bulk rock analyses and ion microprobe in situ analyses. The bulk rock analyses yield 865 ± 50 ppm S in agreement with LA-ICP-MS analyses. These new data support previous estimates of 80% S loss resulting from terrestrial weathering of NWA 7533 pyrite. Pyrite is by far the major S host. Apatite and Fe oxyhydroxides are negligible S carriers, as are the few tiny igneous pyrrhotite–pentlandite sulfide grains included in lithic clasts so far identified. A small nonzero $\Delta^{33}S$ ($-0.029 \pm 0.010‰$) signal is clearly resolved at the 2σ level in the bulk rock analyses, coupled with negative CDT-normalized $\delta^{34}S$ ($-2.54 \pm 0.10‰$), and near-zero $\Delta^{36}S$ ($0.002 \pm 0.09‰$). In situ analyses also yield negative $\Delta^{33}S$ values (-0.05 to $-0.30‰$) with only a few positive $\Delta^{33}S$ up to $+0.38‰$. The slight discrepancy compared to the bulk rock results is attributed to a possible sampling bias. The occurrence of mass-independent fractionation (MIF) supports a model of NWA 7533 pyrite formation from surface sulfur that experienced photochemical reaction(s). The driving force that recycled crustal S in NWA 7533 lithologies—magmatic intrusions or impact-induced heat—is presently unclear. However, in situ analyses also gave negative $\delta^{34}S$ values ($+1$ to $-5.8‰$). Such negative values in the hydrothermal setting of NWA 7533 are reflective of hydrothermal sulfides precipitated from H_2S/HS^- aqueous fluid produced via open-system thermochemical reduction of sulfates at high temperatures (>300 °C).

INTRODUCTION

In the absence of ozone, terrestrial sulfur of Archean age exhibits prominent MIF effects due to UV irradiation of atmospheric SO_2 to form a variety of reduced and oxidized sulfur species (Farquhar et al. 1998, 2002; Pavlov and Kasting 2002). The Martian atmosphere is likely to have had similar UV irradiation

effects on volcanically produced SO_2 over most of Martian history, thus producing MIF in S isotopic signatures (Farquhar et al. 2000; Halevy et al. 2007; Righter et al. 2009). In contrast to Earth, the Martian sulfur cycle may have been dominated throughout its geochemical history by processes operating at the Martian surface due to the lack of an efficient sulfur crustal recycling mechanism (King and McLennan [1990]; Foley et al. [2003]; Franz et al. [2019a]; and references therein). Landers, rovers, and remote sensing observations by orbiting spacecraft using different spectrometers identified a great diversity of Ca-, Mg-, Fe-sulfate minerals as major components of the Martian surface (see a review in Franz et al. 2019a). The abundance and diversity of sulfate minerals testify to a wide range of formation processes such as sulfur output through volcanic outgassing of SO_2 (Tian et al. 2010; Gaillard et al. 2013; Kerber et al. 2015; Franz et al. 2017), oxidation or acid weathering of pre-existing igneous pyrrhotite/pyrite to Fe-sulfates (e.g., Zolotov and Shock 2005; Dehouck et al. 2012), hydrothermal precipitation (e.g., McCubbin et al. 2009), and brines from low pH waters that contained sulfuric acid (e.g., McLennan et al. 2005), to near neutral, low-salinity water that precipitated Ca sulfates by evaporation (e.g., Grotzinger et al. 2014; Nachon et al. 2014). The Curiosity rover has identified Ca-sulfate-bearing fractures of diagenetic origin deposited from near neutral water in the fluvio-lacustrine sedimentary sequence filling the Noachian Gale crater (Grotzinger et al. 2014; Nachon et al. 2014). Thick veins of Ca-sulfate (gypsum) were also identified at Endeavour crater by the Opportunity rover (Squyres et al. 2012). Sulfates of Martian origin were also identified in the interior of Martian meteorites. The Chassigny meteorite shows Ca-sulfate associated with carbonate veins (Wentworth and Gooding 1994). Nakhlite meteorites show evaporitic Ca-sulfate (gypsum, anhydrite) associated with halite, Fe-rich carbonate, saponite, Fe^{3+} oxides, and silica gels, all well preserved in the Nakhla meteorite (Gooding et al. 1991; Bridges and Grady 2000). Jarosite was found in a melt inclusion inside clinopyroxene in MIL 03346 nakhlite (McCubbin et al. 2009). These different sulfates point to episodic periods of water flow that exchanged sulfur processed with the atmosphere and then deposited oxidized sulfur-bearing minerals through fractures, millions of years after complete solidification of the igneous mass (Changela and Bridges [2011]; Bridges et al. [2019]; and references therein). Sulfates were also assimilated into the nakhlite parent magma at the igneous stage, as shown by isotopically anomalous igneous pyrrhotite (Franz et al. 2014; Dottin et al. 2018; Mari et al. 2019) that reequilibrated its metal to sulfur ratios toward metal-

deficient compositions (Chevrier et al. 2011; Mari et al. 2019). The nakhlite meteorites which contain both sulfate and magmatic sulfide minerals display the largest range of MIF anomalies (Farquhar et al. 2007; Franz et al. 2014; Dottin et al. 2018). The Lafayette meteorite, another nakhlite, contains sulfates and/or sulfides with positive $\Delta^{33}S$ anomalies (like the Chassigny meteorite) while Fe sulfides from the 4.1 Ga old orthopyroxenite ALH 84001 display large variations from negative to positive $\Delta^{33}S$ values (-1.10 ± 0.14‰ to 0.66 ± 0.22‰; Farquhar et al. 2000; Franz et al. 2014).

Sulfur isotope exchange between oxidized and reduced forms of sulfur during hydrothermal circulation can also generate large mass-dependent fractionations of S isotopes. Impact-driven hydrothermal activity is thought to explain $\delta^{34}S$ of -9 to -10‰ in carbonate-associated pyrites of the 4.1 Ga old orthopyroxenite ALH 84001 (Shearer et al. 1996). Franz et al. (2017) documented Fe sulfides strongly depleted in ^{34}S ($\delta^{34}S = -47 \pm 14$‰) in the Cumberland (CB) and Oudam (OU) fluvio-lacustrine sediments of Gale crater. These values were interpreted to be produced by equilibrium isotopic fractionation between sulfides and sulfates in groundwater warmed by impact or igneous intrusions (Franz et al. 2017). Regolith breccia NWA 7533 (paired with the so-called "Black Beauty" meteorite NWA 7034 (Agee et al. 2013) and paired stones) that has sampled 4.4 Ga old impact lithologies (Humayun et al. 2013) is of special interest for testing this suggestion of Franz et al. (2017). Unlike SNC meteorites, regolith breccias are almost devoid of magmatic sulfides and contain sulfides of mostly hydrothermal origin (pyrite and scarce pyrrhotite; Lorand et al. 2015). This Ni-rich (up to 4.5 wt% Ni) pyrite is primary unlike other hydrothermal pyrite occurrences so far reported in SNC meteorites and ALH 84001 that are instead the oxidation product of more reduced sulfides (Shearer et al. 1996; Greenwood et al. 2000a, 2000b; Lorand et al. 2018a). This pyrite likely reflects S-rich hydrothermal fluids that percolated through the breccia billions of years after breccia formation (Lorand et al. 2015; Goderis et al. 2016).

Our aim is to address the origin of S in the late circulating fluids using the S budget from both bulk rock S contents and S multi-isotope systematics. We focus on NWA 7533 because it is the only one among the impact breccia samples that have been studied in detail for pyrite distribution and composition including chalcophile trace elements (Lorand et al. 2015, 2018b). The sulfur isotope analyses were done both with digestion of powdered rocks and by ion microprobe in situ measurements on pyrite and pyrrhotite. These data are used to build a comprehensive picture of hydrothermal S cycling in this polymict regolith breccia.

MAIN PETROGRAPHIC FEATURES OF NWA 7533

The petrogenesis of NWA 7533 impact breccia has been reported in a series of recent papers (Wittmann et al. 2015; McCubbin et al. 2016; Hewins et al. 2017). Its impact origin was identified from the rock textures (various lithic clasts and impact melt rocks) and high (up to 1000 ppm Ni, 1 < Ir < 100 ppb) concentrations of siderophile elements (Ni, Ir, and other highly siderophile elements—HSE; Humayun et al. 2013; Wittmann et al. 2015; Goderis et al. 2016). NWA 7533 meteorite was classified as a polymict breccia because it is composed of separate clasts with chemical compositions that require multiple igneous, sedimentary, or impact melt sources (see Hewins et al. [2017] and references therein).

Briefly, its fine-grained interclast matrix (ICM) contains lithic clasts (norite, monzonite) and single mineral clasts derived from these rocks and probably orthopyroxenite, as well as clast-laden melt rocks (CLMR), microbasalt, and melt spherules. Noritic clasts are composed of ferroan pyroxene ($En_{<72}$), orthopyroxene or inverted pigeonite, plagioclase (An_{50-30}), and Cr-rich magnetite. Monzonitic clasts show alkali feldspar, often perthitic, associated with plagioclase ($<An_{30}$), ferroan pyroxene, chlorapatite, and Fe-Ti oxides (magnetite, ilmenite, and accessory rutile). Noritic and monzonitic clasts contain zircon and baddeleyite that may also occur as individual mineral clasts. Zircons in NWA 7533 and paired meteorites yielded pre-Noachian, U-Pb crystallization ages of 4.47–4.35 Ga with a discordance implying a disturbance at around 1.4 Ga (Humayun et al. 2013; Bellucci et al. 2015; McCubbin et al. 2016). Crystal clasts are fragments of disaggregated lithic clasts. Noritic and monzonitic clasts show widespread evidence of impactor-derived contamination: Their concentration levels of siderophile elements (Ni, Ir, etc.) indicate that 3–5% impactor materials accumulated over repeated impact events (Humayun et al. 2013). This pervasive siderophile enrichment in the melt rocks suggests a thick sequence of impact-generated rocks including mature regolith. The monzonite clasts were formed by either differentiation of these large impact melt sheets or remelting of primary Martian crust at depth in the presence of volatiles. A few pyroxene clasts contain exsolution implying prolonged cooling at depth. Another zoned pyroxene population suggests near surface crystallization (Leroux et al. [2016]; Hewins et al. [2017]; and references therein).

Microbasalts and CLMR clasts show closely similar bulk composition and similar siderophile element enrichment (Humayun et al. 2013). CLMRs are composed of plagioclase laths and subophitic pyroxene indicating rapid quenching due to incorporation of abundant clasts. Microbasalts are composed of orthopyroxene (En_{73-63}) or pigeonite (En_{63-49}), augite (En_{46-29}), plagioclase (An_{66-30}), and Fe-rich spinel. Because of their subophitic to granoblastic textures, microbasalts are interpreted as impact melt that crystallized less rapidly than CLMR (Hewins et al. 2017). Regarding lithophile trace element geochemistry, the spherules, the groundmass of the melt rock, and the microbasalts resemble melted windblown dust and regolith debris (Humayun et al. 2013). The dense ICM consists of anhedral micrometer-sized plagioclase embedded in submicrometer-sized pyroxene, plus fine-grained Fe-(Ti) oxides—magnetite and maghemite (Muttik et al. 2014; Leroux et al. 2016). Disturbances in several isotopic systems (U-Pb in zircon; K-Ar/Ar-Ar; Pb-Pb in phosphates; bulk rock Re/Os systematics) indicate a probable major reheating event that annealed the breccia at 1.35–1.4 Ga (Humayun et al. 2013; Bellucci et al. 2015; Goderis et al. 2016; McCubbin et al. 2016; Hewins et al. 2017; Cassata et al. 2018; see also Leroux et al. 2016).

SULFIDE MINERALOGY OF NWA 7533

The sulfide mineralogy in NWA 7533 impact breccia was previously studied from the seven polished sections (7533-1 to -7) and one doubly polished transparent thick section (7533-LM) available at the Museum National d'Histoire Naturelle (MNHN; Lorand et al. 2015). NWA 7533 is unique among Martian meteorites in being almost devoid of the magmatic sulfide assemblage of igneous origin (i.e., pyrrhotite–pentlandite–chalcopyrite) repeatedly reported in SNC meteorites (e.g., Lorand et al. 2005, 2018a; Chevrier et al. 2011; Franz et al. 2014; Baumgartner et al. 2017; Dottin et al. 2018; Franz 2019a, 2019b; Mari et al. 2019). Ni-bearing pyrrhotite (3 wt% Ni) + pentlandite was identified only as three inclusions in plagioclase clasts over the eight polished thick sections investigated. By contrast, accessory pyrite (0.6–1% by weight according to an X-ray distribution map of S and point counting estimates) is widespread and evenly distributed in all of the impact lithologies (monzonitic and noritic clasts, CLMR, melt spherules, and microbasalts), in orthopyroxenite clasts from the pristine Martian crust, as well as in ICM and the late veins cutting across the meteorite. Hence, pyrite is a late-stage mineral that crystallized after the final assembly of the breccia, during the annealing and lithification event presumed to have occurred 1.4 Ga ago (Lorand et al. 2015).

Pyrite crystals show combinations of cubes, truncated cubes, and octahedra (average grain size 30–40 μm). These euhedral crystals were observed mostly
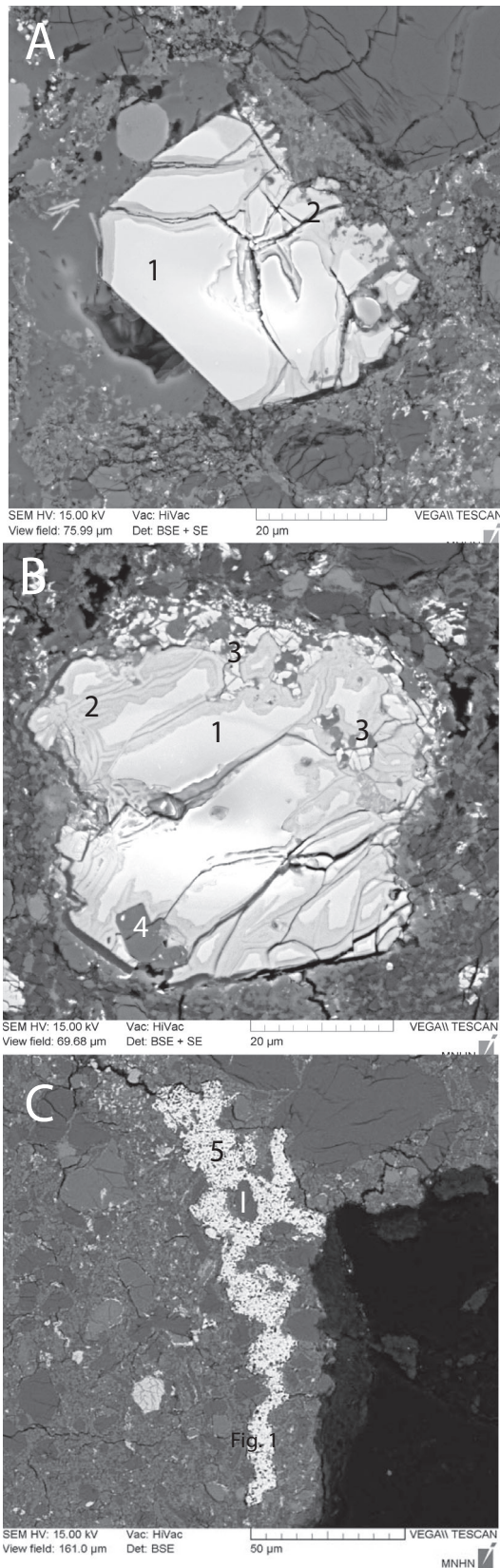
Fig. 1. Backscattered electron (BSE) images of NWA 7533 Fe sulfides. A) euhedral pyrite (1) affected by late fracturing that also guided terrestrial weathering (2) dark gray Fe oxyhydroxides; (B) poikilitic pyrite surrounded by a fine-grained dust of ICM minerals; solid inclusions are skeletal Fe oxides (maghemite-magnetite; (3) and perfectly euhedral apatite (4); (C) interstitial porous pyrrhotite (5) within interclast matrix (ICM). Note silicate clast inclusions (I) in the pyrrhotite.

inside open cracks, microbasalts, and ICM (Fig. 1A). In addition to occurring as euhedral crystals, many pyrites are anhedral grains, sometimes of very small size (down to 1 μm across), especially when disseminated inside ICM (Fig. 1B). Some anhedral pyrite grains replace low-Ca pyroxene clasts. Whether euhedral or anhedral, many pyrite grains are poikiloblastic and enclose relict micron-sized Fe-(Ti) oxides identified as being the same composition and habit as the magnetite–maghemite that is so abundant in NWA 7533 (Fig. 1B). Pyrite-producing reactions thus involved sulfidation, either from magnetite/maghemite, from the low-Ca pyroxene, or from dissolved divalent iron in a fluid. Regardless of their mode of formation, NWA 7533 pyrite grains show nickel-rich areas (up to 4.5 wt%; EMPA and SEM data) representing former Fe-Ni metal particles, as well as highly siderophile element-rich micro-inclusions (Os, Ir, Ru, Pt, Pd, Re, Mo) interpreted as altered impactor debris of the pre-Noachian meteoritic bombardment (Lorand et al. 2015, 2018b). It was inferred from this maximum Ni content (positively correlated with Se) that pyrite started crystallizing at 400–500 °C. Compared to pyrite, hydrothermal pyrrhotite is very scarce, always anhedral, and highly spongy (see Fig. 1C). The assemblage pyrite–pyrrhotite–magnetite and maghemite defines Eh-pH conditions of hydrothermal fluids as near neutral H_2S-HS-rich (6 < pH < 10) oxidizing fluids (minimum log fO_2 of >FMQ + 2 log units; Lorand et al. 2015) in agreement with the redox conditions deduced from pyroxene clast decomposition into Mg-rich pyroxene, silica, and Fe oxide (Leroux et al. 2016). Hydrothermal alteration under oxidizing conditions appears to have given rise to fine-grained Fe-rich phases influencing the magnetic properties of the breccia (Gattacceca et al. 2014).

Pyrite, a very fragile mineral, shows planar fractures (Fig. 1) resembling planar deformation features (PDF). The shock creating such planar fractures was a very late event, because pyrite was one of the last phases to crystallize in the breccia on Mars (Lorand et al. 2015). The fractures were possibly related to the excavation event that liberated the meteorite from the Martian subsurface crust, yet its shock intensity could not be

determined due to the lack of olivine and quartz (Hewins et al. 2017). These fractures acted as preferential pathways for partial replacement of pyrite by iron oxyhydroxides of terrestrial origin according to their D/H values and their distribution defining an alteration gradient throughout the meteorite (Lorand et al. 2015). Electron microprobe analyses (EMP) of altered and hydrated regions in pyrite show compositions similar to that of goethite, but containing ~4% SiO_2 while electron diffraction data indicate the presence of hematite, as well. These oxide mixtures will be treated as iron oxyhydroxides in the present paper (see table S20 in Hewins et al. 2017).

ANALYTICAL METHODS

The bulk analyses of the meteorite were performed on two powder splits (BB UMD 1 and BB UMD 2) of 0.6 g each. Both replicates yielded very similar results in terms of S contents and S isotopic compositions (see below), so we assume that these powder splits were representative of the entire breccia. Bulk sulfur abundances and sulfur isotopic compositions of the bulk sulfur fractions were obtained at the University of Maryland, according to a technique described in detail in Labidi et al. (2012). Briefly, powdered samples were digested in Teflon vessels while continuously flushed with pure N_2. Twenty milliliters of 2.1 M $CrCl_2$ solution and 5 ml of 29 N HF (48%, ultrapure) were used to digest the samples. The H_2S released in this process was flushed to a sulfide trap filled with $AgNO_3$ solution (0.3 M) where it reacted to precipitate Ag_2S. After each extraction and for all samples, weighed Ag_2S precipitate is compared to the S content obtained with EMP and used to determine extraction yields. Weighed silver sulfide samples were subsequently wrapped in Al-foil and placed in Ni reaction vessels for fluorination with at least 10 times excess of pure F_2 at 250 °C overnight. The SF_6 produced was isolated from impurities using cryogenic and chromatographic techniques. The volume of purified SF_6 was then measured with a manometer and transferred to the dual inlet of a ThermoFinnigan MAT 253 isotope ratio gas source mass spectrometer that was used to measure ion beams at m/z = 127+, 128+, 129+, and 131+. Once δ^nS values are determined (n = 33, 34, 36), $\Delta^{33}S$ and $\Delta^{36}S$ are calculated ($\Delta^{33}S = \delta^{33}S - 1000[(\delta^{34}S/1000 + 1)^{0.515} - 1]$ and $\Delta^{36}S = \delta^{36}S - 1000[(\delta^{34}S/1000 + 1]^{1.90} - 1)$. IAEA S1 values are used to evaluate our long-term accuracy and precision on standards, and to anchor our $\delta^{34}S$ to the V-CDT scale. Analyses of the S1 standard performed along with the Mars rock analyses yield average $\delta^{34}S$, $\Delta^{33}S$, and $\Delta^{36}S$ values of $-5.28 \pm 0.09‰$, $+0.083 \pm 0.008‰$, and $-0.78 \pm 0.26‰$

(n = 13, all 2 s.d.) relative to our reference gas (see details in Labidi et al. 2017). Relative to the same reference gas, our CDT yield $\delta^{34}S$, $\Delta^{33}S$, and $\Delta^{36}S$ values at $-4.88 \pm 0.15‰$, $-0.035 \pm 0.008‰$, and $-0.08 \pm 0.08‰$ (n = 6, all 2 s.d.). The S isotope shift for $\delta^{34}S$, $\Delta^{33}S$, and $\Delta^{36}S$ between CDT and S1 is comparable to what was obtained elsewhere (Ohno et al. 2006; Labidi et al. 2012). We use the CDT scale to anchor our $\delta^{34}S$, $\Delta^{33}S$, and $\Delta^{36}S$ values. We additionally report our $\delta^{34}S$ values on the V-CDT scale to allow comparisons with other data sets that also reported $\delta^{34}S$ values relative to V-CDT (e.g., terrestrial mantle-derived rocks; Labidi et al. 2012). We obtained 2σ uncertainties of 0.10, 0.012, and 0.25‰ for $\delta^{34}S$, $\Delta^{33}S$, and $\Delta^{36}S$ values, respectively, for all measurements with an SF_6 amount >1 μmol.

The in situ analyses of S multi-isotopes were done with ion probes on two polished thin sections (7533-4 and 7533-5) over the eight available. These two polished thin sections show unaltered pyrite crystal cores large enough to be analyzed. The dimensions and localization of the final ion microprobe spots were checked with a scanning electron microscope (Tescan VEGA II LSU scanning electron microscope [SEM]) operating in conventional (high-vacuum) mode, and equipped with an SD3 (Bruker) EDS detector (Muséum National d'Histoire Naturelle Paris, France = MNHN) operating in the backscattered mode (BSE; see Lorand et al. [2015] for more details). Major element compositions of pyrite (Fe, Ni, S) were determined with the same standardless eEnergy dispersive procedure as in Lorand et al. (2015) inside the ion beam craters of SIMS analysis; these latter analyses agree quite well with pyrite compositions reported in Lorand et al. (2015, 2018b).

Two Cameca IMS 1280 facilities (CRPG, Nancy, France; NordSIMS facility, Stockholm, Sweden; Table 1) were used. The analytical method for the CRPG Cameca IMS 1280 HR2 is described in detail in Thomassot et al. (2009) and in Muller et al. (2016). Sulfur isotope compositions of sulfides from thick section 7533-5 were measured by simultaneous measurements of $^{32}S^-$, $^{33}S^-$, $^{34}S^-$, and $^{36}S^-$ in multicollection mode with three off-axis Faraday cups (L′2, C, and H1) that were intercalibrated before each session of analyses, and one electron multiplier (H2) for the most rare isotope (^{36}S). The analytical settings were 5 nA, Cs^+- primary beam focused to a spot of about 15 μm, with secondary intensities from 8.2×10^8 to 10.2×10^8 cps for ^{32}S, depending on the mineralogy. Gains and backgrounds of the Faraday cups were regularly measured during the entire session. Measurements were performed with an automatic centering process and consist of 30 cycles of 4 s each

Table 1. S isotopic compositions of sulfides in NWA 7533 (Canyon Diablo-normalized).

	S (ppm)	$\delta^{34}S$ (‰)	2σ	$\Delta^{33}S$ (‰)	2 σ	$\Delta^{36}S$ (‰)	2σ
Bulk rock (U Maryland)							
BB-UMD-1	920	−2.39	0.013	−0.026	0.012	0.002	0.105
BB-UMD-2	805	−2.673	0.027	−0.031	0.01	0.001	0.076
Average	863	−2.532	0.015	−0.029	0.010	0.002	0.09
NWA 7533-4 (NORDSIMS)							
Site 8a Pyrite		−1.82	0.23	−0.34	0.17	0.08	0.53
Site 8b Pyrite		−2.5	0.23	−0.36	0.18	0.12	0.66
Site 5b Pyrite		−1.54	0.18	−0.21	0.12	0.03	0.44
Site 15 Pyrite		−2.5	0.17	−0.12	0.14	0.49	0.51
Site 16a Pyrite		−1.63	0.17	−0.21	0.14	−0.55	0.53
Site 16b Pyrite		−3.25	0.17	−0.05	0.14	−0.43	0.49
Site 17 Pyrite		−2.99	0.18	−0.16	0.13	−0.004	0.45
Site b1a Pyrite		−2.22	0.19	−0.16	0.16	−0.083	0.54
Site b1b Pyrite		−1.5	0.17	−0.13	0.14	−0.39	0.53
Site 9a Pyrrhotite		−1.65	0.38	−0.19	0.28	0.12	0.81
Site 9b Pyrrhotite		−1.61	0.41	−0.14	0.28	0.39	0.71
Site 11 Pyrrhotite		−3.16	0.4	−0.26	0.3	0.05	0.6
Site 12 Pyrrhotite		−3.11	0.32	−0.28	0.23	0.49	0.67
Average		−2.22		−0.186		0.01	
2SD		1.38		0.18		0.66	
wtd. Av. (95% conf.)		0.41		0.044		0.20	
MSWD		42.		1.11		1.4	
NWA 7533-5 (Nancy)							
Site A Pyrite		−1.71	0.32	−0.01	0.18	0.59	0.48
Site 8 Pyrite		0.6	0.32	−0.22	0.18	0.03	0.48
Site-1a Pyrite		−0.44	0.32	−0.17	0.18	0.57	0.48
Site-1b Pyrite		−2.49	0.32	−0.12	0.18	0.3	0.48
Site-17 Pyrite		−0.11	0.32	−0.12	0.18	0.15	0.48
Site-19 Pyrite		0.39	0.32	−0.13	0.18	0.37	0.48
Site-12 Pyrite		−0.79	0.32	−0.04	0.18	−0.49	0.48
Site-C Pyrite		−4.02	0.32	−0.1	0.18	−0.21	0.48
Site-6-1 Pyrite		−1.33	0.32	0.11	0.18	−0.74	0.48
Site 6-2 Pyrite		−0.75	0.32	−0.18	0.18	−0.15	0.48
Site-B1 Pyrite		−1.21	0.32	−0.38	0.18	−2.27	0.48
Site G Pyrite		−5.08	0.32	−0.08	0.18	−2.22	0.48
Site-F-1 Pyrite		−1.57	0.32	−0.09	0.18	−0.4	0.48
Site-F-2 Pyrite		−0.19	0.32	−0.11	0.18	−0.92	0.48
Site F-4 Pyrite		−5.58	0.32	0.35	0.18	0.26	0.48
Site 16-1 Pyrite		−2.01	0.32	0.24	0.18	0.02	0.48
Average*		−1.65		−0.12		0.32	
2SD		3.69		1.5		1.74	
wtd. av. (95% conf.)		0.98		0.064		0.46	
MSWD		132		1.5		13.0	

2SD is the simple 2× standard deviation on the values (measures variation in a data set regardless of individual run uncertainties).

wtd.av. is the weighted average uncertainty on the data along its MSWD value (measures the spread).

*Exclude the positive values of D33S in Site F-4 Pyrite and Site 16-1 Pyrite.

after a pre-sputtering time of 300 s. The background of the detectors was measured during the pre-sputtering and was then used to correct each analysis. The internal precision achieved under these conditions was better than 0.05‰ for $\delta^{34}S$ and 0.03‰ for $\delta^{33}S$ values (2σ). The external precision, determined from repeated measurements on various reference materials, was 0.40‰ (2σ) for $\delta^{34}S$, 0.09‰ (2σ) for $\Delta^{33}S$ values, and 0.24‰ for $\Delta^{36}S$. Several pyrite in-house reference materials (Maine, Philippot et al. 2012; Balmat pyrite, courtesy of M. Whitehouse; and Spain-CR, Muller et al. 2016) were used to determine (1) the instrumental mass fractionation and (2) the reference mass discrimination line, from which $\Delta^{33}S$ and $\Delta^{36}S$ values were calculated. The values of the in-house reference materials can be found in Muller et al. (2017). The bulk

isotopic compositions of these materials were measured by conventional gas source mass spectrometer at IPGP following Labidi et al. (2012).

Quadruple S-isotopes were measured in situ on section 7533-4 at an approximately 10 µm scale using a CAMECA ims1280 SIMS instrument (NordSIMS Facility, Stockholm), closely following analytical protocols outlined by Whitehouse (2013). The sulfur isotopes ^{32}S, ^{33}S, and ^{34}S were measured on Faraday detectors, while ^{36}S was measured on an ion counting electron multiplier, corrected for drift using interspersed reference materials (Balmat and Ruttan pyrites), which were also used to correct for instrumental mass bias. Isua pyrite was used to monitor the mass independent values.

Sulfur contents of Fe oxyhydroxides and apatite that may be potential S reservoirs (e.g., Parat et al. 2011) were analyzed in situ using a laser ablation inductively coupled plasma mass spectrometer— LA-ICP-MS) at the "Laboratoire de Planétologie et Géodynamique" in Nantes (France) following the procedure described in detail by Lorand et al (2018b). The samples were ablated and analyzed for ^{34}S using a Bruker 880 quadrupole ICP-MS coupled with a Photon Machine Analyte™ G2 equipped with an excimer laser (193 × nm laser wavelength) and a dual volume sample cell that keeps the sample volume small and constant. The laser was operated with a repetition rate of 10 × Hz and a laser output energy of 90 × mJ with a 50% attenuator and 20× demagnification, resulting in low fluences on the sample (<4 J m^{-2}). Spot sizes for standards and samples were set to 25–50 µm depending on the size of the mineral grains. Six Fe oxyhydroxide grains replacing pyrite were analyzed in section 7533-5 with a spot size of 25 × µm, NIST 610 glass as calibration standard, and SiO$_2$ content as internal standard, based on the values published by Lorand et al. (2015) and Hewins et al. (2017). Eight apatite crystals from NWA 7533-5 were analyzed with a laser spot size of 50 µm, NIST 612 glass as calibration standard, and Ca as internal standard based on the apatite analyses reported by Hewins et al. (2017). Concentrations in both cases were determined using Glitter™ software (Table 2).

RESULTS

The two bulk rock analyses yield quite reproducible bulk S concentrations (805–920 ppm). These bulk chemistry values are very close to the mean value calculated from LA-ICP-MS raster analyses of Humayun et al. (2013) although the latter method detected huge variations (100–1500 ppm) between each of the breccia components (CLIMR, ICM, microbasalts, melt spherules), reflecting small-scale variations in modal abundances and weathering degrees of pyrite (Lorand et al. 2015, 2018b). The samples yield an average Δ^{33}S of $-0.029 \pm 0.010‰$ reflecting a small but resolvable nonzero signal in Δ^{33}S at the 2σ level. This nonzero Δ^{33}S is coupled with negative δ^{34}S ($-2.54 \pm 0.10‰$). The NWA 7533 meteorite S isotopic composition is distinct from that of the juvenile Martian S isotopic composition calculated by Franz et al. (2019a) from 47 shergottite analyses (δ^{34}S = $-0.24 \pm 0.05‰$, Δ^{33}S = $0.0015 \pm 0.0016‰$, Δ^{36}S = $0.039 \pm 0.054‰$).

In addition to bulk isotope measurements, 29 spot analyses were performed on 18 pyrite and 3 pyrrhotite grains of sufficient size (>20 µm) that were not significantly altered to Fe-oxyhydroxides. Ion microprobe measurements yielded more negative Δ^{33}S values ($-0.05 < \Delta^{33}$S $< -0.38‰$) compared to the bulk rock analyses, and a wider range of negative δ^{34}S signatures ($-1.5 < \delta^{34}$S $< -3.1‰$; with outliers up to -5.5 and $+0.6‰$; Fig. 2). The Nancy SIMS analyses show a larger scatter in the δ^{34}S and Δ^{33}S values than the bulk analyses and include two positive values for Δ^{33}S (0.24–$0.35‰$ corresponding to Site 16-1 and Site F-4 pyrites; Table 1). The ranges of Δ^{36}S are similar: -0.55 to $+0.49‰$ (NORDSIMS) versus -0.9 to $+0.49‰$ (Nancy SIMS), excluding one outlier at $-2.2‰$ (**Site B-1** Pyrite). Correlation between Δ^{33}S and δ^{34}S is lacking (Fig. 2). There are no correlations between sulfur isotopic compositions and pyrite Ni contents (<0.1–3 wt%; Table 1; Fig. 3), suggesting that the correction procedure of SIMS analyses was not affected by the small deviation of NWA 7533 pyrite compared to pure FeS$_2$. The spread in the δ^{34}S values seems to be due to beam overlap over polymineralic aggregates (pyrite-Fe oxides or Fe oxyhydroxides), matrix silicates or vein-filling terrestrial products (calcite). The analyses having incorporated some calcite seem to shift δ^{34}S toward more positive values (7533-5-19; 7533-5-17; 7533-5-F-2; 7533-5-1a; Fig. 1). No systematic trend can be seen for those analyses overlapping Fe oxyhydroxides or matrix silicates (δ^{34}S down to $-55.58‰$ for NWA7533-5-G).

The six pyrite crystals analyzed with the NORDSIMS ion microprobe show a very similar range of negative Δ^{33}S values ($-0.05‰ < \Delta^{33}$S $< -0.36‰$) to the 12 Nancy SIMS pyrite analyses; however, with no positive values. Both data sets also yield consistent results with regard to the negative δ^{34}S value of NWA 7533 sulfides ($-3.3‰ < \delta^{34}$S $< -1.5‰$). Duplicate analyses generated variable reproducibility that reflected the different degrees of sulfide alteration from one section to another (e.g., site 16a,b; Table 1), and the grain size of the preserved pyrite. Pyrite and the three

Table 2. Laser ablation inductively coupled mass spectrometry (LA-ICPMS) analyses of pyrite alteration products.

	1 LA-ICPMS	2 LA-ICPMS	3 LA-ICPMS	4 LA-ICPMS	5 LA-ICPMS	6 LA-ICPMS	EMPA ($n = 15$)*
Fe oxyhydroxides (pyrite alteration products)							
S (ppm)	2392	2059	3061	4128	3728	2299	2400 ± 1300
Ca	4455.5	13,158.6	10,681.2	5349.9	11,609.4	8009.6	9500 ± 2015
Sr	79.5	75.6	372.3	386.2	411.3	283.4	
Ba	227.1	91.1	198.2	283.6	271.6	233.6	
Detection limits							
S (ppm)	2.83	3.09	4.48	4.14	7.76	3.77	
Ca	3.68	4.17	6.20	5.82	11.20	5.81	
Sr	0.001	0.001	0.002	0.002	0.004	0.002	
Ba	0.009	0.009	0.014	0.013	0.027	0.014	
	0.003	0.003	0.005	0.005	0.010	0.004	

	1 LA-ICPMS	4 LA-ICPMS	6 LA-ICPMS	7 LA-ICPMS	8 LA-ICPMS	9 LA-ICPMS	10 LA-ICPMS	11 LA-ICPMS
Apatite								
S (ppm)	229.9	230.2	209.3	217.2	229.6	231.1	267.6	351.9
Ca	IS	IS	IS	IS	IS	IS	IS	IS
Sr	137.3	157.6	145.6	112.7	179.9	197.7	143.9	171.4
Ba	6.73	8.98	8.05	5.09	7.28	12.4	5.13	11.33
Detection limits								
S (ppm)	2.01	2.81	2.40	3.37	3.10	3.42	3.87	4.33
Sr	0.001	0.001	0.001	0.001	0.009	0.001	0.001	0.001
Ba	0.006	0.009	0.007	0.009	0.008	0.009	0.011	0.010

IS = internal standard.

*Electron Microprobe analyses—EMPA (Lorand et al., 2015).

highly spongy pyrrhotite grains of hydrothermal origin analyzed here carry similar isotopic compositions at the two-sigma level (Table 1; Fig. 2). Due to their lower count rate, the NordSIMS analyses of pyrrhotite are less precise compared to the analyses of pyrite, as shown by the two-sigma values of the three S isotope ratios. This lower precision may result from the highly spongy nature of that pyrrhotite, showing pore sizes much smaller (<1 μm) than the ion beam diameter (>10 μm).

DISCUSSION

At first sight, the occurrence of mass-independent fractionation of sulfur (S-MIFs) supports a Martian origin for sulfur in NWA 7533 as deduced from microtextural and compositional characteristics of NWA 7533 pyrite (Lorand et al. 2015). Indeed, S-MIFs are generated by UV-induced photochemical processes in an atmosphere poor in O_2 like the Martian atmosphere since the earliest times (e.g., Farquhar et al. 2000, 2001; Pavlov and Kasting 2002). In oxygen isotopes, MIF effects also affect the bulk rock composition of NWA 7034 (Agee et al. 2013), phosphates (Belluci et al. 2020), and are largest in NWA 7533 zircons (Nemchin et al. 2014).

Moreover, the variation in $\Delta^{33}S$ with an absence of significant anomalies in $\Delta^{36}S$ (Fig. 4) is considered to be diagnostic of S-MIF production on Mars, by different pathways from those that operated on the early Earth and in Earth's stratosphere today (see e.g., Masterson et al. 2011). The calculated mean $\Delta^{36}S$ value from both the bulk rock and SIMS analyses is close to 0‰, a characteristic feature of S multi-isotope systematics of Martian meteorites compared to Archean terrestrial samples showing mass-independent signatures (Franz et al. 2014, 2019a, 2019b; Fig. 4). The plot in Fig. 4 also rules out alternative fractionation processes, such as, for example, mass-dependent fractionation during Rayleigh distillation with alternative mass laws (e.g., Young et al. 2002). This latter process should produce a regression line characterized by a slope of -7 ± 1 whereas our data set does not align on any correlation at all. However, it is worth noting that all but three analyses of NWA 7533 sulfides plot within the scattergram of nakhlites in the $\Delta^{36}S$ versus $\Delta^{33}S$ plot of Fig. 4. This may be more than a coincidence because NWA 7533 sulfides were dated at 1.4 Ga, like nakhlites that recorded sulfate contamination at each stage of their petrogenetic history (e.g., Franz et al. 2014; Dottin et al. 2018; Lindsay, personal communication). This could reflect the S
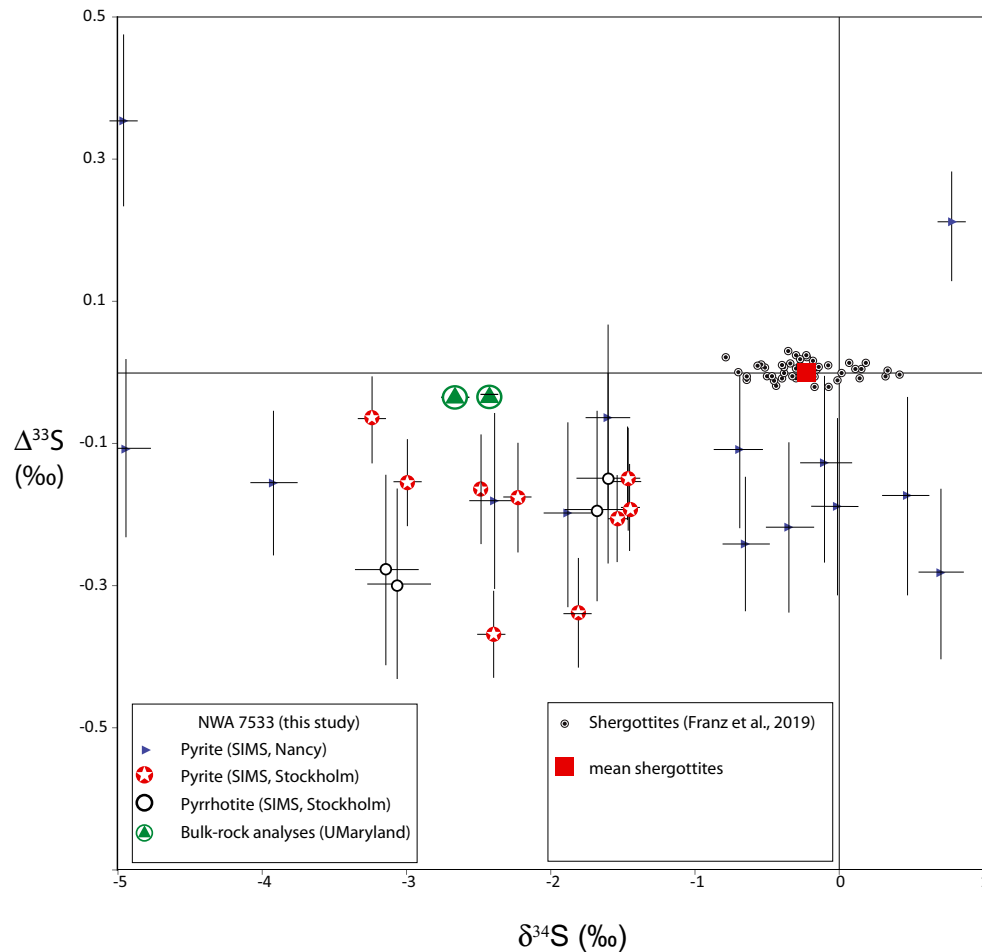
Fig. 2. $\delta^{34}S$ versus $\Delta^{33}S$ diagram for NWA 7533 sulfides and bulk rock. $\Delta^{33}S = \delta^{33}S - 1000*\ ([\delta^{34}S/1000 + 1]0.515 - 1)$. Compositional field of shergottites and weighted mean used as revised estimate for the juvenile Martian sulfur composition after Franz et al. (2019b), excluding the samples that were described as contaminated by crustal materials. Note the overall negative $\delta^{34}S$ values of NWA 7533 sulfides for slightly negative $\Delta^{33}S$ values compared to shergottites. Typical error bars on shergottite data display 2σ uncertainties. (Color figure can be viewed at wileyonlinelibrary.com.)

isotopic composition of surficial sulfur at that time on the Martian crust, or a specific S reservoir sampled by both Martian breccias and nakhlites.

The presence of sulfur isotopic variations that are both mass-independent and mass-dependent compared to the inferred composition of Martian mantle-derived sulfur argues in favor of a crustal origin of NWA 7533 pyrite consistent with its hydrothermal origin (Lorand et al. 2015). Even taking into account only the bulk rock data, the small but significant negative $\Delta^{33}S$ values overlap with the isotopic S compositions reported for some shergottites that are now considered to have assimilated crustal sulfur (NWA 11300; NWA 7635; Franz et al. 2019a). Before further discussion, it is necessary to address any bias in the database. Hence, the following three points will be addressed (1) how can the slight discrepancy between in situ analyses and bulk rock determination of $\Delta^{33}S$ be explained, (2) how was

anomalous S transferred to impact breccias, and (3) what was the ultimate process that triggered hydrothermal cycling of S in these Martian regolith breccias.

The Balance of the Bulk Rock S Multi-Isotope Budget of NWA 7533

Anomalous $\Delta^{33}S$ for pyrite was observed with two different ion microprobes in two different laboratories. This argues for a significant negative $\Delta^{33}S$ anomaly as measured by SIMS, which seems to conflict with the near-zero $\Delta^{33}S$ value of $-0.029 \pm 0.010‰$ measured with precise bulk S isotope measurements. It is not the first time that in situ analyses and bulk rock determination of S isotopes do not match. Franz et al. (2014) documented quite a large discrepancy between SIMS analyses and chemical extractions of MIL 03346 pyrrhotite ($\Delta^{33}S = -0.73 \pm 0.13$ versus $-0.43‰$) but
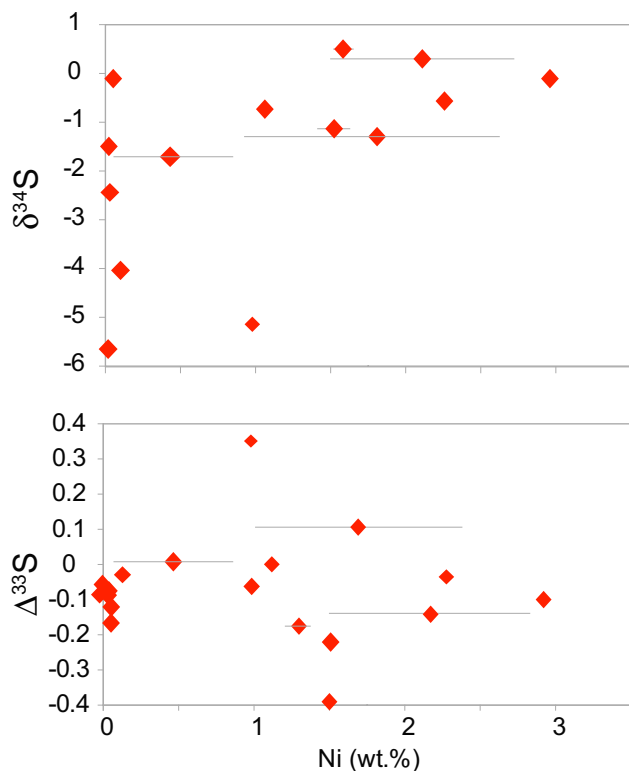
Fig. 3. $\Delta^{34}S$ versus Ni and $\Delta^{33}S$ versus Ni diagrams for NWA 7533 pyrite (NWA7533-5; SEM analyses for Ni). (Color figure can be viewed at wileyonlinelibrary.com.)

did not propose a reason for the discrepancy. Dottin et al. (2018) also reported SIMS analyses of nakhlites paired with MIL 00336 yielding lower $\Delta^{33}S$ compared to bulk rocks, and argued that the SIMS measurements captured a different population of sulfides than the bulk analyses. Another possible source of analytical bias is that S-bearing phases other than the two Fe-sulfides, pyrrhotite and pyrite, were overlooked by petrographic studies.

Sulfur in NWA 7533 was identified as residing in both magmatic sulfide assemblages, apatite and Fe-oxyhydroxides (Lorand et al. 2015; this study). As said before, the impact breccia is almost devoid of magmatic sulfides, which is interpreted to result from repeated impact and shock melting. It is well known that shock melts are strongly degassed (Pierazzo and Artemieva 2012; Righter et al. 2015). Nickel, a strongly chalcophile element, was demonstrated to behave as a lithophile element in impact melt derived noritic and monzonitic clasts that crystallized without evolving sulfide melts (Hewins et al. [2017] and references therein). The paucity of magmatic sulfides in NWA 7533 clearly reflects the repeated heavy bombardment of the Martian regolith. Another potential S carrier in igneous rocks is apatite (Parat et al. 2011) which is a late magmatic mineral in

lithic clasts and microbasalts of the breccia (Hewins et al. 2017). NWA 7533 apatite S content determined by LA-ICP-MS is quite homogeneous (200–300 ppm; Table 2). However, apatite is a minor mineral (<6 vol% in NWA 7034, paired with NWA 7533; Agee et al. 2013) and its contribution to the whole rock S budget is expected to be negligible (<15 ppm versus 865 ppm). Its effect on the S isotopic composition is difficult to predict without a reliable apatite standard for SIMS isotope analyses. However, we can speculate that magmatic sulfides or apatite containing juvenile Martian sulfur would drive the S multi-isotope composition of NWA 7533 toward 0‰ in the $\delta^{34}S$ versus $\Delta^{33}S$ diagram of Fig. 2. Alternatively, Humayun et al. (2014) suggested that NWA 7533 lithic clasts crystallized from impact melts that incorporated already weathered clay-rich Martian soils. In that case, evidence from SNC meteorites and analyses of Gale crater sulfates (Greenwood et al. 2000a, 2000b; Farquhar et al. 2007; Franz et al. 2014, 2017, 2019a; Dottin et al. 2018; Mari et al. 2019) predict deviation of $\delta^{34}S$ toward strongly positive values in Fig. 2. Clearly, neither magmatic sulfides nor apatite could account for the dilution of the pre-existing nonzero $\Delta^{33}S$ at near constant $\delta^{34}S$ between in situ SIMS analyses and the two bulk rock data.

Fe oxyhydroxides contain 10 times more S than does apatite (3000 ± 1000 ppm; now measured in situ with both EMP and LA-ICP-MS, Table 2). However, simple mass balance calculations suggest that Fe oxyhydroxides are a negligible S reservoir, too. They would represent approximately 40 ppm S (5% of the bulk rock S concentration) at best taking into account the highest in situ measured S content (≈4000 ppm) and modal abundances of approximately 1 wt% (implying a total oxidation of pyrite, which is an overestimate). Some of the sulfur of Fe oxyhydroxides may come from both oxidized pyrites and terrestrial sources with near-zero $\Delta^{33}S$ values, which would explain the shift in the bulk rock $\Delta^{33}S$ values compared to ion microprobe data. From the mass balance calculations, Fe oxyhydroxides would have to have unrealistically positive $\Delta^{33}S$ of about +6 to +9‰ to explain the shift of $\Delta^{33}S$ from −0.2 ± 0.1‰ (SIMS data) relative to the bulk value of −0.03 ± 0.01‰.

Sulfates, also major S-bearing phases on Mars (Franz et al. [2017, 2019a] and reference therein), have not been detected in Martian breccia NWA 7533 despite careful SEM scanning of the eight polished pieces studied so far (Lorand et al. 2015; Hewins et al. 2017). There are no coupled Ba + S spikes that could correspond to barite micro-inclusions in the time-resolved diagram of the LA-ICP-MS analyses of Fe oxyhydroxides (Fig. 5). Barium was systematically detected along with S (in agreement with EMP and
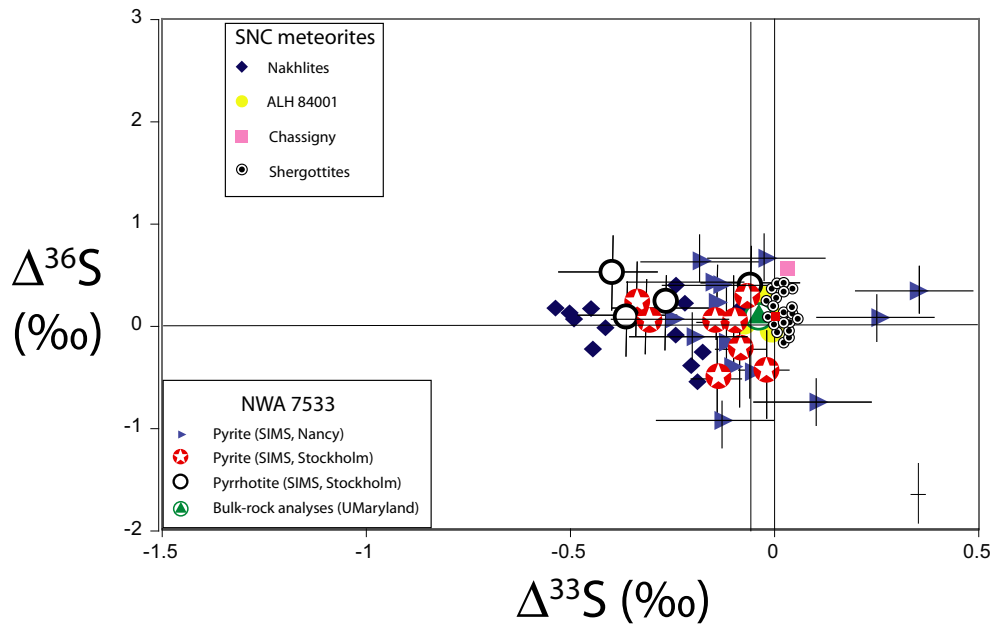
Fig. 4. $\Delta^{33}S$ versus $\Delta^{36}S$ diagrams for NWA 7533 sulfides. $\Delta^{36}S = \delta^{36}S-1000* ([\delta^{34}S/1000 + 1]1.9-1)$. Data for SNC meteorites from Franz et al. (2014, 2019a 2019b). (Color figure can be viewed at wileyonlinelibrary.com.)
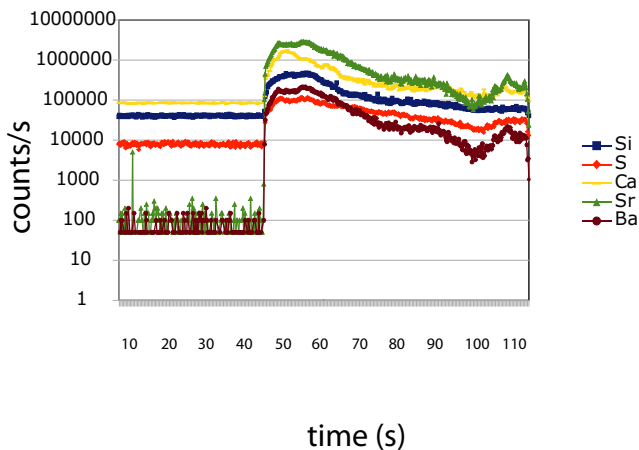

Fig. 5. Time-resolved LA-ICPMS spectra collected along the laser traverse through an Fe oxyhydroxide pseudomorph replacing pyrite.

TEM data for Ca, S, and Si). The Sr and Ba ion signals are highly correlated and the ^{34}S signal follows the Ba and Sr signals very closely in the first portion of the scan in Fig. 5, while the Ca signal is independent of the Ba-Sr-S signals. The high Sr might indicate that an Sr-Ba sulfate is the only sulfate present and that it is sufficiently widely distributed at a nanometric scale in the Fe oxyhydroxides not to form discrete spikes. However, the trend of strongly decreasing S/Se ratio in NWA 7533 Fe oxyhydroxides ($137 < $ S/Se $ < 1193$) compared to their pyrite precursors ($3500 < $ S/

Se $ < 54,000$) supports the hypothesis of extensive leaching of sulfates from the breccia during terrestrial weathering (Fig. 6). Such a drop in the S/Se ratios is consistent with the well-documented differences in the behavior of S and Se in terrestrial weathering (e.g., Lorand et al. [2003] and references therein). Under acidic conditions that characterize terrestrial weathering, both Se^{4+} and Se^{6+} tend to adsorb onto naturally occurring Fe oxides and oxyhydroxides while S is leached as SO_4^{2-} (e.g., Ziemkievics et al. 2011). From pyrite modal abundance (up to 1 wt%; Lorand et al. 2015), NWA 7533 should show a bulk rock S content of 5400 ppm S instead of 865 ± 80 ppm measured in the present study. This suggests a loss of 80% S as dissolved sulfates during terrestrial weathering, which is consistent with previous estimates, either based on pyrite/Fe oxyhydroxide modal ratios (Lorand et al. 2015) or in situ analyses of pyrite S and Se contents (Lorand et al. 2018b).

The discussion above casts serious doubt on whether another S reservoir with a significant effect on bulk S isotopic composition is present in these breccias. Another possible source of discrepancy between the bulk rock analyses and in situ measurements is analytical bias generated by one or both of the two techniques. The bulk rock analysis involved an extraction procedure of S using a Cr(II) solution (cf. Labidi et al. 2012) which has been shown to be very inefficient for sulfates (Gröger et al. 2009). However, this analytical bias was likely negligible because as
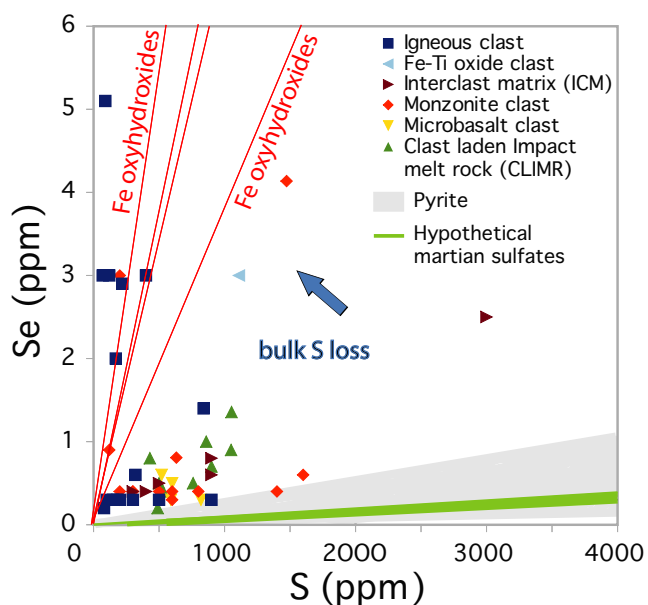
Fig. 6. Se versus S plots for NWA 7533. Color symbols correspond to the rastered LA-ICPMS analyses of the different lithological components of NWA 7533 (Humayun et al. 2013). NWA pyrite and Fe oxyhydroxide compositions from Lorand et al. (2018b). The blue arrow depicts the preferential leaching of S with respect to Se resulting from terrestrial weathering. Putative composition of Martian sulfates after Wang and Becker (2017). (Color figure can be viewed at wileyonlinelibrary.com.)

shown above, NWA 7533 meteorite lacks detectable amounts of sulfates. A systematic analytical bias from both the Nancy and Stockholm SIMS can be ruled out because multiple sulfur analyses were processed in both places the same way using the same reference materials and both were mass resolved from $^{32}S^1H$. One may speculate that hydride generation could be a bit higher on the sulfide standard mount block (in epoxy; or if the standard sulfides themselves are hydrated) than on the meteorite section, thus generating $\Delta^{33}S$ values biased toward higher values that would in return make the unknowns lower in $\Delta^{33}S$. Another effect that could alter the $\Delta^{33}S$ values measured by SIMS is the Faraday amplifier background drift. Many of the sulfides analyzed in our paper are yielding somewhat lower 70–80% count rates than the standards, so a small drift would have a disproportionate effect in any drift correction, probably at around the 0.1‰ level (around 1000 cps in 10^7 cps), and it would lower $\Delta^{33}S$ too. However, there is no direct evidence that this putative drift might have operated during the analytical session of NWA 7533 sulfides. Moreover, the background was systematically measured during the pre-sputtering time.

The question that arises now is whether the SIMS analyses sampled one or several S populations from the same sulfides (pyrite and/or pyrrhotite). This issue can be addressed by looking at the uncertainty data on the average triple S compositions reported in Table 1 as the simple 2× standard deviation on the values, and the weighted average uncertainty on the data, along with its MSWD value. Both the NORDSIMS and Nancy data set yield similar results:

- Large spread of data for $\delta^{34}S$ (MSWD of 42 for the NORDSIMS analyses and 132 for the Nancy analyses), beyond what can be explained by analytical uncertainties. This scatter could represent a real mass-dependent fractionation (MDF) trend or a subtle analytical issue. Hence, the weighted average uncertainty is obviously not a useful measure of the scatter for $\delta^{34}S$ that integrates a component of geological scatter (MDF).
- $\Delta^{33}S$ values define statistically single low MSWD (1.1 versus 1.5 for the Nancy and NORDSIMS data set, respectively) populations that are very slightly negative. In fact, combining both data sets gives a weighted average of −0.165 ± 0.032‰, not overlapping the bulk value. Of course, the fact that $\delta^{34}S$ shows variation means that our analyses may have sampled two (or more) reservoirs that are very slightly different in $\Delta^{33}S$. Testing that interpretation from a $\Delta^{33}S$ versus $\delta^{34}S$ plot would demand many more analyses with much better individual data uncertainties than we have. In that case, the calculation with standard deviations may apply, which would give a mean $\Delta^{33}S$ value of −0.2 ± 0.18 (2SD) for the Stockholm data, −0.12 ± 0.22 (2SD) for the Nancy data, and a − 0.16 ± 0.11 (2SD) for the combined data set. Taken individually, both mean $\Delta^{33}S$ values overlap the bulk rock data, but when combined, they do not.
- Our $\Delta^{36}S$ averages are similar to each other and within error of the bulk. However, the Nancy data display a greater spread (MSWD of 13) perhaps inconsistent with sampling a single population.

To summarize, the fact that SIMS and bulk rock data do not overlap at 95% confidence suggests that the two techniques may have sampled different sulfur isotopic compositions from the same Fe-sulfides, assuming that each data set (the UMD bulk rock data, the NordSIMS data, and the Nancy data) are single populations. Thus, the case for multiple S populations could be stronger than the case for analytical bias. Deciphering which parameter really played the major role in our data set is made difficult by the fact that we are comparing data at the 0.1‰ level, which is very close to the limitations of the SIMS method. We also cannot exclude that the tiny pyrite crystals that are well below the size of the SIMS beam (1 versus 10 μm, respectively) in impact breccia NWA 7533 show less
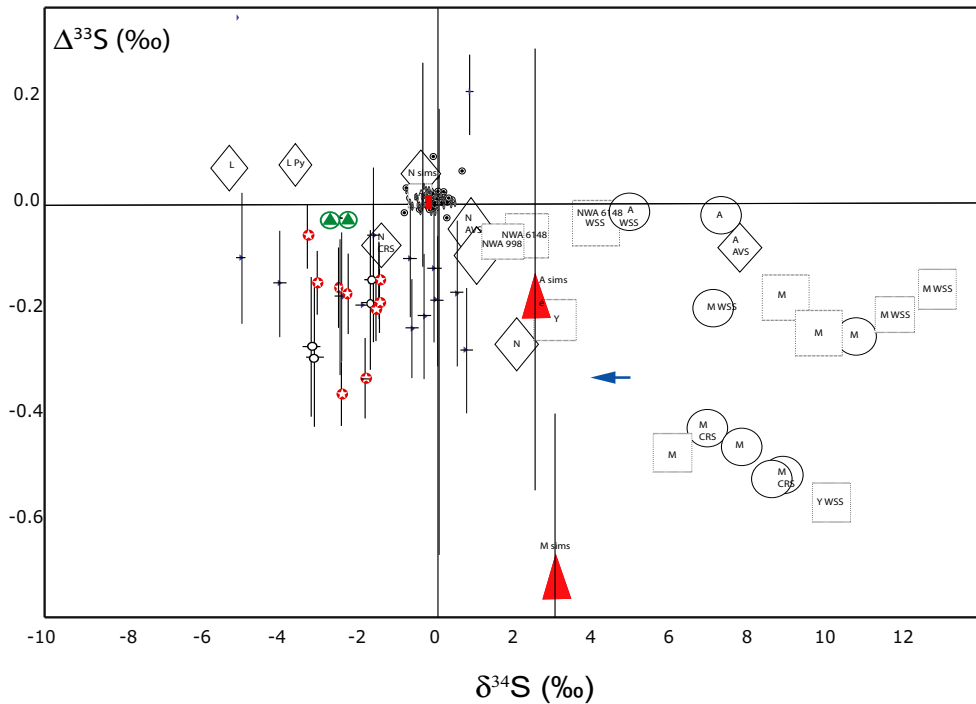
Fig. 7. Comparison of NWA 7533 pyrite compositions with SNC meteorites in a $\delta^{34}S$ versus $\Delta^{33}S$ diagram. A = ALH 84001; L = Lafayette; N = Nakhla; Y = Y000593 (nakhlite); M = Miller Range nakhlites; NWA 998 and NWA 6148: nakhlites; WSS, water-soluble sulfates; AVS, acid-volatile sulfides; CRS, Chromium-reducible sulfides; Py, pyrite. Other caption as in Fig. 3. bulk rock analyses. Note the overall negative $\delta^{34}S$ values of NWA 7533 sulfides for slightly negative $\Delta^{33}S$ values compared to nahklite sulfates. Arrow materializes possible thermochemical reduction of sulfates into NWA 7533 hydrothermal sulfides. (Color figure can be viewed at wileyonlinelibrary.com.)

negative $\Delta^{33}S$ compared to the larger crystals measured. Clearly, resolving both issues will demand better spatial resolution and analytical precision than those of present-day SIMS techniques.

Hydrothermal Cycling of MIF-Bearing S in NWA 7533

As recalled in the introduction, SNC meteorites that have sampled subeffusive igneous rocks of the Martian crust (i.e., nakhlites) have provided multiple evidence of crustal S contamination that took place throughout the cooling history of these rocks, from the magma crystallization stage to late exposure to hydrothermal fluids and evaporitic brines (see also Dottin et al. 2018; Bridges et al. 2019; Franz et al. [2019a, 2019b]; and references therein). These rocks produce trends of positive $\delta^{34}S$ values coupled with negative $\Delta^{33}S$ values with water-soluble (Ca sulfates) and acid-soluble sulfates (jarosite) in Antarctic nakhlites (McCubbin et al. 2009) defining the highest $\delta^{34}S$ endmembers (Fig. 7). Likewise, ALH 84001 (a proxy of NWA 7533 orthopyroxene crystal clasts with similar ages of formation; Hewins et al. 2017) incorporated crustal sulfate enriched in ^{34}S along with anomalous ^{33}S

($\delta^{34}S = 7.20 \pm 0.15\%_0$, $\Delta^{33}S = -0.072 \pm 0.008\%_0$, $\Delta^{36}S = 0.02 \pm 0.15\%_0$; Franz et al. 2014). We note here that the MIF observed in NWA 7533 (this study) and in the nakhlites (Franz et al. 2014; Dottin et al. 2018) are an order of magnitude smaller than the effects observed in terrestrial Archean pyrites (Farquhar et al. 2000). During the photolysis of SO_2, the magnitude of the S-MIF effect is dependent on the formation of at least two distinct species, an oxidized sulfate (or gaseous SO_3) and a reduced sulfur polymer (S_2 or S_8) between which the sulfur isotopes are distributed in a mass-independent manner (Pavlov and Kasting 2002). The presence of oxidation on Mars' surface evidenced by oxychlorine compounds would oxidize the reduced species, so that practically all sulfur ends up as sulfate at the surface. This would prevent the formation of large MIF effects in surficial sulfate, contrary to initial expectations.

As suggested by NWA 7533 pyrite, negative $\delta^{34}S$ values seem to be a characteristic feature of pyrite occurrences in SNC meteorites. Shearer et al. (1996) and Greenwood et al. (2000a, 2000b) documented a wide range of $\delta^{34}S$ ($-9.69 \pm 0.22\%_0$ to $7.8 \pm 0.7\%_0$), as well as anomalous $\Delta^{33}S$ signals ($-0.74 \pm 0.39\%_0$

and $-0.51 \pm 0.38\%$) in two pyrite grains located in "crushed zones" of ALH 84001 and associated with carbonates interpreted to have hydrothermal origin. Negative $\delta^{34}S$ values were also published for Lafayette pyrite resulting from partial replacement of pyrrhotite by sulfur-bearing fluid influx into the nakhlite unit (Greenwood et al. 2000a, 2000b; Fig. 7). The same is true for Chassigny pyrite that replaced pyrrhotite ($-4.6\% < \delta < -1.5\%$; Greenwood et al. 2000a, 2000b). According to Shearer et al. (1996) and Greenwood et al. (2000a, 2000b), igneous pyrrhotite in ALH 84001 was largely converted to pyrite by a secondary alteration process, such as an impact-driven hydrothermal system. A low-temperature (200 °C) hydrothermal influx of volatile components (S, C, H) was postulated for this reaction in Chassigny, too (Floran et al. 1978; Lorand et al. 2018a; Peslier et al. 2019; and references therein). Using results from the sample analysis at Mars (SAM) facility aboard the Curiosity rover, Franz et al. (2017) found large variations in $\delta^{34}S$ in 10 sites of fluvio-lacustrine sediments filling the Gale crater that exceed those measured for Martian meteorites. They identified quite low $\delta^{34}S$ ($-47 \pm 14\%$) at both Cumberland (CB) and Oudam (OU) sites where sulfides (pyrrhotite, pyrite) occur and enrichment in ^{34}S ($0 < \delta^{34}S < 28 \pm 7\%$ [CDT normalized]) in mudstone-hosted sulfates. They concluded that sulfur isotopic equilibrium between sulfides and sulfates could have been reached through warmed groundwater within several thousand years at 100–150°C to yield $\delta^{34}S$-depleted sulfides.

A similar process known as thermochemical sulfate reduction (TSR) is assumed to have transferred S-MIF-bearing S into Martian impact breccias. TSR is associated with kinetic fractionation that scales with temperature (Kiyosu and Krouse 1990). Anhydrite–pyrite fractionation coefficients indicate a difference of 15‰ at 300 °C (Shanks [2014] and references therein) with more positive (heavier) compositions in sulfates compared to pyrite. Typical TSR S isotope fractionations are usually less than 20‰ (Machel et al. 1995; Seal 2006). A crude estimate for initial Martian sulfate source enriched in ^{34}S is suggested by $\delta^{34}S$ as high as $4.7 \pm 0.2\%$ in sulfate extracted from Nakhla (Farquhar et al. 2007). Shergottite sulfates show $\delta^{34}S$ of $6.68 \pm 0.15\%$ (Farquhar et al. 2007). Higher values recorded by sulfate of Antarctic nakhlites MIL 03346 and its pairs (up to 12.39‰) may reflect input of terrestrial sulfates (Franz et al. 2014), but are not unrealistic for Martian sulfates as suggested by analyses of sulfate in fluvio-lacustrine sediments of Gale crater (Franz et al. 2017). Hence, taking into account the extreme isotopic composition of Martian sulfates, the isotopic fractionation relationship between NWA 7533 pyrite and putative Martian sulfates ($\delta^{34}S_{sulfate - pyrite}$) is

about 10‰. Such $\delta^{34}S$ values require TSR temperatures in excess of 250 °C using the experimentally derived equation of Kiyosu and Krouse (1990; see also Machel et al. 1995). To preserve negative $\delta^{34}S$ values, this system must have been open with respect to the supply of sulfate (sulfate supply > sulfate consumption), otherwise pyrite would develop positive $\delta^{34}S$ values upon completion of closed system fractionation effects (e.g., Magnall et al. 2016). Such an open system is consistent with the widespread distribution of pyrite inside porosity of each lithological component of Martian breccias, including late veinlets. The TSR process may have contributed along with other petrogenetic processes (magma degassing, weathering, etc.) to the highly oxidized state of NWA 7533 of ~FMQ + 2 log units (Leroux et al. 2016; Hewins et al. 2017), well above typical Martian magmatic conditions. Reduction of one mole of S^{6+} to S^{2-} consumes eight moles of electrons and has the potential to oxidize eight moles of Fe^{2+} to Fe^{3+} (see detailed calculation in Dottin et al. 2018). Our scenario of precursor sulfates is also supported by the S/Se ratio of NWA 7533 pyrite (3500–54,000; Lorand et al. 2018b; Fig. 5). Selenium chemistry is strongly tied to S chemistry: both elements can substitute as anions into sulfides while forming oxycompounds hosted in sulfates (Howard 1977; Huston et al. 1995; Lorand et al. 2003; Ziemkievics et al. [2011] and references therein). Although Se concentration data (and hence S/Se ratio) are not available for Martian sulfates, one nakhlite (MIL 03346) that bears multiple evidence of Martian sulfate contamination shows a bulk rock S/Se ratio of up to 13,385 whereas it is only 3566 ± 798 for the shergottites that have incorporated juvenile (mantle-derived) Martian sulfur (Wang and Becker 2017). Owing to its S/Se ratio up to 54,000, there can be little doubt that NWA 7533 pyrite formed from precursor sulfates (Fig. 6).

The Eh-pH redox conditions deduced for NWA 7533 from the Fe-S-O system, and the lack of any firmly identified sulfate, imply that sulfate reduction products were recycled by hydrothermal fluids in the Martian breccia as reduced to near-neutral H_2S/HS^--rich aqueous fluids (Lorand et al. 2015). Reduction of sulfate during the hydrothermal process would generate H_2S and potentially H_2Se that are likely to precipitate as pyrite in the presence of Fe^{2+} (Auclair et al. 1987). Experimental studies on terrestrial hydrothermal vent systems demonstrate that at 300 and 350 °C (a temperature range corresponding to that deduced from the Ni content of NWA 7533 pyrite; Lorand et al. 2015, 2018b), pyrite is expected to be depleted in the heavy isotopes of S relative to H_2S at equilibrium (Seal 2006; Wu et al. 2010; Gregory et al. 2015; Magnall et al.

2016). Lorand et al. (2015, 2018b) suggested that NWA 7533 pyrite precipitated by direct nucleation or sulfidation reactions between H_2S/HS^--rich aqueous fluids and Fe from different sources (dissolved ions in the fluid, pyroxene clast, matrix oxides [magnetite, maghemite]). Like pyrite, the negative $\Delta^{33}S$ coupled with negative $\delta^{34}S$ values makes the few fine-grained spongy anhedral pyrrhotite grains identified in the interclast matrix (ICM) of NWA 7533 crystallization products from fluids that reduced crustal sulfates (Fig. 2). However, the highly resorbed and denticulated shape of these pyrrhotite blebs and their spongy textures compared to euhedral pyrite crystals are noteworthy. Such sulfide textures were reported in SNC meteorites that experienced shock-induced sulfur degassing (Lorand et al. 2012; Gattaceca et al. 2013). Lorand et al. (2012) concluded that pyrite in the strongly shocked chassignite NWA 2737 was desulfurized into FeS due the high shock pressure (55 GPa) coupled with strong heating conditions (perhaps up to 800 °C) published for this meteorite. In NWA 7533, the shock event postdating pyrite crystallization generated only PDFs in pyrite. A desulfurization of pyrite into spongy pyrrhotite is thus considered to be very unlikely. For comparison, pyrite was preserved in Chassigny that experienced a shock pressure of much greater intensity (about 35 GPa with a post-shock temperature of about 300 °C; Lorand et al. 2018a). The NWA 7533 spongy pyrrhotite must be interpreted as a metastable hydrothermal product of sulfate reduction reactions reflecting local, transient more reducing conditions during percolation by hydrothermal fluids (see Lorand et al. 2015).

Meteorite Impact Versus Igneous Intrusion as Source of NWA 7533 Hydrothermal Pyrite?

According to a detailed analysis of pyrite textures and its relationships with silicate lithologies of NWA 7533, hydrothermal alteration took place at a very late stage of the history of the meteorite during and after a lithification and annealing event that made the regolith breccia very cohesive. This annealing event responsible for the lithification of the meteorite likely occurred at ~1.4 Ga from the apatite U-Pb ages (Bellucci et al. 2015), the zircon lower intercept ages and the K-Ar ages (Humayun et al. 2013; Lindsay et al. 2014; McCubbin et al. 2016; Cassata et al. 2018) and the whole rock $^{187}Re/^{187}Os$ model ages (Goderis et al. 2016). Taking into account the Amazonian age of NWA 7533 pyrite, the water responsible for the hydrothermal event on Mars was likely produced by melting of ice from a subsurface permafrost reservoir. Chlorine was likely present too, as indicated by core–rim increase in Cl/F

ratio of NWA 7533 apatite (Belluci et al. 2015); however, Lorand et al. (2018b) suggested that the chlorine content was significantly low when NWA 7533 pyrite precipitated because this sulfide shows very low contents of the base metals (Cu, Zn, etc.) that are preferentially transported by Cl-rich acidic fluids. This hydrothermal cycling process bears similarities to that documented for nakhlites from the Fe-carbonate + Ca-sulfates + halite veins: Changela and Bridges (2011) argued for an impact-induced heating event which triggered upward percolation of H_2O-CO_2 fluids from buried ice into the nahklite igneous mass, although both upward and downward percolations were also suggested (see Bridges et al. [2019] and references therein). A downward percolation of sulfate-bearing aqueous fluid is considered to be more likely for Martian impact breccias; however, the source of heat that triggered this percolation, either an impact or a magmatic event is still debated (Lindsay, personal communication).

Meteorite impacts on rocky planetary bodies have the potential to initiate transient hydrothermal systems if (1) the target contains sufficient volatiles (e.g., liquid water or ice), and (2) a substantial heat source is generated (e.g., melt sheet, nearby pluton, raised geothermal gradient; Newsom 1980; Abramov and Kring 2005; Naumov 2005; Osinski et al. 2013; Koeberl 2014). Sulfides are common hydrothermal products in impact craters on Earth and mineralization dominated by pyrite is thought to occur during the latest stages of cooling (Simpson et al. 2005, 2017; Parnell et al. 2010). Geochemical modeling of impact-generated hydrothermal systems for Mars also frequently returns pyrite among hydrothermal products (e.g., Schwenzer and Kring 2013). As shown by these authors, pyrite becomes a major mineral along with hematite for water/rock ratios exceeding 1000. Such conditions are met inside veins, as observed in NWA 7533 where some cracks are filled with pyrite + maghemite (Lorand et al. 2015). Cassata et al. (2018) proposed for NWA 7034 (paired with NWA 7533) a rather different interpretation linking the lithification and annealing event with a thermal dome above deeper intrusives because thermal metamorphism recorded by the K-Ar and U-Pb systems yields plateau age differences that were greater than durations (10s of Ma or less) required to cool shock-heated basement terrains following large (100–200 km) impact events that might have occurred at ~1300 Ma. Magmatism is known to have occurred on Mars at 1.4–1.35 Ga from the nakhlite and chassignite meteorites (Nyquist et al. [2001]; Cohen et al. [2017] and references therein), while the impact cratering rate of the Martian surface was already considerably reduced at that time (e.g., Moser et al. 2019). However, MacArthur et al. (2019) related the maximum ^{40}Ar-^{39}Ar age of

J.-P. Lorand et al.

1130–1250 Ma in the NWA 8114 meteorite clast (paired with NWA 7533) analyzed by them to an impact shock event and the subsequent high-temperature oxidative breakdown of many of the pyroxenes (also documented in NWA 7533 by Leroux et al. 2016). A simple Fourier cooling model suggested that a burial depth of 5 m was enough to maintain sufficiently high temperatures (>600 °C) for ~30 days (MacArthur et al. 2019). With this constraint in hand, one may assume that sulfates in Martian breccias may have been reduced to sulfides almost in situ, implying very little transport of aqueous fluids.

CONCLUSIONS

Pyrite is by far the major host of sulfur in the polymict NWA 7533 breccia and paired meteorites. Apatite and Fe oxyhydroxides are negligible S carriers, as are the tiny magmatic sulfide grains so far identified. Sulfates (barite or gypsum) have not been firmly identified in the breccia. The initial sulfur content of the breccia inferred from the modal abundance of pyrite and its pseudomorphous Fe oxyhydroxides is estimated to be ~5400 ppm. The two bulk rock S analyses obtained here confirm previous estimates of 80% S loss resulting from terrestrial weathering of NWA 7533 pyrite.

The occurrence of S-MIF in the S multi-isotope composition supports a model of NWA 7533 pyrite formation from Martian surficial sulfur that experienced photochemical reaction(s). The slight discrepancy between in situ SIMS analyses ($\Delta^{33}S = -0.2 \pm 0.1\permil$; mean of 29 analyses) and the bulk IRMS analyses ($\Delta^{33}S = -0.029 \pm 0.010\permil$) is tentatively interpreted as a likely sampling bias since only grains> 20 μm in size were analyzed.

Negative $\delta^{34}S$ values were previously reported for several occurrences of secondary pyrite in SNC meteorites. Such negative values in the hydrothermal setting of NWA 7533 are reflective of authigenic sulfide precipitated from H_2S produced via open-system reduction of sulfates. A transient more reducing stage likely produced the spongy pyrrhotite that carries similar S multi-isotope compositions as that of pyrite.

It is concluded that sulfur was recycled by downward percolation of reduced S-bearing aqueous fluid produced by melting of permafrost. However, the driving force that recycled crustal S in NWA 7533 lithologies, underlying magmatic intrusions or impact-induced heating, is presently unclear.

Acknowledgment—We are indebted to L. Labenne for the sample. We are grateful for funding from CNES-INSU grant 2014-PNP (J.-P. L.) and the Agence Nationale de la Recherche (ANR) under the contract ANR16CE310012 entitled Mars Prime. The LA-ICP-MS facility at the LPG Nantes was established by funds from the Region Pays de la Loire. Carole La is thanked for her help with the LA-ICP-MS facility at LPG Nantes; MH was supported by NASA Solar System Workings (NNX16AP98G). The National High Magnetic Field Laboratory is supported by the National Science Foundation through NSF/DMR-1644779 and the state of Florida. The revised version was greatly improved thanks to comments from three reviewers and editorial suggestions from Cyrena Goodrich.

Editorial Handling—Dr. Cyrena Goodrich

REFERENCES

Abramov O. and Kring D. A. 2005. Impact-induced hydrothermal activity on early Mars. *Journal of Geophysical Research* 110:E12S09. https://doi.org/10.1029/2005JE002453.

Agee C. B., Wilson N. V., McCubbin F. M., Ziegler K., Polyak V. J., Sharp Z. D., Asmerom Y., Nunn M. H., Shaheen R., Thiemens M. H., Steele A., Fogel M. L., Bowden R., Glamoclija M., Zhang Z., and Elardo S. M. 2013. Unique meteorite from Early Amazonian Mars: Water-rich basaltic breccia Northwest Africa 7034. *Science* 339:780–785.

Auclair G., Fouquet Y., and Bohn M. 1987. Distribution of selenium in high-temperature hydrothermal sulfide deposits at 13° North, East Pacific Rise. *Canadian Mineralogist* 25:577–588.

Baumgartner R., Fiorentini M., Lorand J.-P., Baratoux D., Zaccarini F., Ferrière L., Prasek M., and Sener K. 2017. The role of sulfides in the fractionation of highly siderophile and chalcophile elements during the formation of Martian shergottite meteorites. *Geochimica et Cosmochimica Acta* 210:1–24.

Bellucci J. J., Nemchin A. A., Whitehouse M. J., Humayun M., Hewins R., and Zanda B. 2015. Pb-isotopic evidence for an early, enriched crust on Mars. *Earth & Planetary Science Letters* 410:34–41.

Bellucci J. J., Whitehouse M. J., Nemchin A. A., Snape J. F., Kenny G. G., Merle R. E., Bland P. A., and Benedix G. K. 2020. Tracing Martian surface interactions with the triple O isotope compositions of meteoritic phosphates. *Earth & Planetary Science Letters* 531:115977.

Bridges J. C. and Grady M. M. 2000. Evaporite mineral assemblages in the nakhlite (Martian) meteorites. *Earth & Planetary Science Letters* 176:267–279.

Bridges J., Hicks J. M., and Treiman A. H. 2019. Carbonates on Mars. In *Volatiles in the Martian crust*, edited by Filiberto J. and Schwenzer S. P. Amsterdam: Elsevier. pp. 89–118.

Cassata W. S., Cohen B. E., Mark D. F., Trappitsch R., Crow C. A., Wimpenny J., Lee M. R., and Smith C. L. 2018. Chronology of Martian breccia NWA 7034 and the formation of the Martian crustal dichotomy. *Science Advances* 4:eaap8306.

Changela H. G. and Bridges J. C. 2011. Alteration assemblages in the nakhlites: Variation with depth on Mars. *Meteoritics & Planetary Sciences* 45:1847–1867.

Chevrier V., Lorand J.-P., and Sautter V. 2011. Sulfide petrology of four nakhlites (NWA817, NWA998, Nakhla, Governador Valadares). *Meteoritics & Planetary Science* 46:769–784.

Cohen B. E., Mark D. F., Cassata W. S., Lee M. R., Tomkinson T., and Smith C. L. 2017. Taking the pulse of Mars via dating of a plume-fed volcano. *Nature Communications* 8:640.

Dehouck E., Chevrier V., Gaudin A., Mangold N., Mathe P. E., and Rochette P. 2012. Evaluating the role of sulfide-weathering in the formation of sulfates or carbonates on Mars. *Geochimica et Cosmochimica Acta* 90:47–63.

Dottin J. W., Labidi J., Farquhar J., Piccoli P., Liu M.-C., and McKeegan K. D. 2018. Evidence for oxidation at the base of the nakhlite pile by reduction of sulfate salts at the time of lava emplacement. *Geochimica et Cosmochimica Acta* 239:186–197.

Farquhar J., Savarino J., Jackson T. L., and Thiemens M. H. 2000. Evidence of atmospheric sulfur in the Martian regolith from sulfur isotopes in meteorites. *Nature* 404:50–52.

Farquhar J., Savarino J., Airieau S., and Thiemens M. H. 2001. Observation of wavelength-sensitive mass-independent sulfur isotope effects during SO_2 photolysis: Implications for the early atmosphere. *Journal of Geophysical Research* 106:32,829–32,839.

Farquhar J., Kim S.-T., and Masterson A. 2007. Implications from sulfur isotopes of the Nakhla meteorite for the origin of sulfate on Mars. *Earth Planetary Science Letters* 264:1–8.

Floran R. J., Prinz M., Hlava P. F., Keil K., Nehru C. E., and Hinthorne J. R. 1978. The Chassigny meteorite: A cumulate dunite with hydrous amphibole-bearing melt inclusions. *Chemical Geology* 42:1213–1222.

Foley C. N., Economou T., and Clayton R. N. 2003. Final chemical results from the Mars Pathfinder Alpha Proton X-ray Spectrometer. *Journal of Geophysical Research* 108:8096. https://doi.org/10.1029/2002JE002019.

Franz H. H., Kim S. T., Farquhar J., Day J. M. D., Economos R. C., McKeegan K., Schmitt A. K., Irving A. J., Hoek J., and Dottin J. III. 2014. Isotopic links between atmospheric chemistry and the deep sulfur cycle on Mars. *Nature* 508:365–368.

Franz H. B., McAdam A., Ming D. W., Freissinet C., Mahaffy P. R., Eldridge D. L., Fischer W. F., Grotzinger J. P., House C. H., Hurowitz J. A., McLennan S. M., Schwenzer S. P., Vaniman D. T., Archer P. D., Jr Atreya S. K., Conrad P. G., Dottin J. W. I. I. I., Eigenbrode J. L., Farley K. A., Glavin D. P., Johnson S. S., Knudson C. A., Morris R. V., Navarro-Gonzalez R., Pavlov A. A., Plummer R., Rampe E. B., Stern J. C., Steele A., Summons R. E., and Sutter B. 2017. Large sulfur isotope fractionations in Martian sediments at Gale crater. *Nature Geoscience* 10:658–662.

Franz H. B., King P. L., and Gaillard F. 2019a. Sulfur on Mars from the atmosphere to the core. In *Volatiles in the Martian crust*, edited by Filiberto J. and Schwenzer S. P. Amsterdam: Elsevier. pp. 119–183.

Gaillard F., Michalski J., Berger G., McLennan S. M., and Scaillet B. 2013. Geochemical reservoirs and timing of sulfur cycling on Mars. *Space Science Review* 174:251–300.

Gattacceca J., Hewins R. J., Lorand J.-P., Rochette P., Lagroix F., Cournède C., Uehara M., Pont S., Sautter V., Scorzelli R. B., Hombourger C., Munayco P., Zanda B., and Chennaoui H. 2013. Opaque minerals, magnetic properties and paleomagnetism of the Tissint Martian meteorite. *Meteoritics & Planetary Science* 48:1919–1936.

Gattacceca J., Rochette P., Scorzelli R. B., Munayco P., Agee C., Quesnel Y., Cournède C., and Geissman J. 2014. Martian meteorites and Martian magnetic anomalies: A new perspective from NWA 7034. *Geophysical Research Letters* 41:4859–4864. https://doi.org/10.1002/2014GL060464.

Goderis S., Brandon A. D., Mayer B., and Humayun M. 2016. Ancient impactor components preserved and reworked in Martian regolith breccia Northwest Africa 7034. *Geochimica et Cosmochimica Acta* 191:203–215.

Gooding J. L., Wentworth S. J., and Zolensky M. 1991. Aqueous alteration of the Nakhla meteorite. *Meteoritics* 326:135–143.

Greenwood J. P., Mojzsis S. J., and Coath C. D. 2000a. Sulfur isotopic compositions of individual sulfides in martian meteorites ALH 84001 and Nakhla: Implications for crust-regolith exchange on Mars. *Earth & Planetary Science Letters* 184:23–35.

Greenwood J. P., Riciputi L.R., McSween H. Y. Jr., and Taylor L. A. 2000b. Modified sulfur isotopic compositions of sulfides in the nakhlites and Chassigny. *Geochimica et Cosmochimica Acta* 64:1121–1131.

Gregory D. D., Large R. R., Halpin J. A., Steadman J. A., Hickman H. E., Ireland T. E., and Holden P. 2015. A degree of sulfate reduction in an open system to produce negative $\delta^{34}S$. *Geochimica et Cosmochimica Acta* 150:223–250.

Gröger J., Franke J., Hamer K., and Schulz H. D. 2009. Quantitative recovery of elemental sulfur and improved selectivity in a chromium-reducible sulfur distillation. *Geostandards and Geoanalytical Research* 33:17–27.

Grotzinger J. P., Sumner D. Y., Kah L., Stack C. K., Gupta S., Edgar L., Rubin D., Lewis K., Schieber J., Mangold N., Milliken R., Conrad P. G., DesMarais D., Farmer J., Siebach K., Calef K., Hurowitz J., McLennan S. M., Ming D., Vaniman D., Crisp J., Vasavada A., Edgett K. S., Malin M., Blake D., Gellert R., Mahaffy P., Wiens R. C., Maurice S., Grant J. A., Wilson S., Anderson R. C., Beegle L., Arvidson R., Hallet B., Sletten R. S., Rice M., Bell J. III, Griffes J., Ehlmann B., Anderson R. B., Bristow T. F., Dietrich W. E., Dromart G., Eigenbrode J., Fraeman A., Hardgrove C., Herkenhoff K., Jandura L., Kocurek G., Lee S., Leshin L. A., Leveille R., Limonadi D., Maki J., McCloskey S., Meyer M., Minitti M., Newsom H., Oehler D., Okon A., Palucis M., Parker T., Rowland S., Schmidt M., Squyres S., Steele A., Stolper E., Summons R., Treiman A., Williams R., and Ayingst, MSL Science Team 2014. A habitable fluvio-lacustrine environment at Yellowknife Bay, Gale crater, Mars. *Science* 343: 1–14.

Hewins R. H., Zanda B., Humayun M., Nemchin A., Lorand J.-P., Pont S., Deldicque D., Bellucci J. J., Beck P., Leroux H., Marinova M., Remusat L., Göpel C., Lewin E., Grange M., Kennedy A., and Whitehouse M. 2017. Regolith breccia Northwest Africa 7533: Mineralogy and petrology with implications for early Mars. *Meteoritics & Planetary Sciences* 52:89–124.

Howard J. H. 1977. Geochemistry of Se: Formation of ferroselite and Se behavior in the vicinity of oxidizing sulfide and uranium deposits. *Geochimica et Cosmochimica Acta* 41:1665–1678.

Humayun M., Nemchin A., Zanda B., Hewins R. H., Grange M., Kennedy M., Lorand J.-P., Göpel C., Pont S., Fieni C., and Deldicque D. 2013. Origin and age of the earliest Martian crust from meteorite NWA 7533. *Nature* 503: 513–516.

Humayun M., Hewins R. H., Lorand J.-P., and Zanda B. 2014. Weathering and impact melting determined the mineralogy of the early Martian crust preserved in Northwest Africa 7533 (abstract #1880). 45th Lunar and Planetary Science Conference. CD-ROM.

Huston D. L., Sie S. H., Suter G. F., Cooke D. R., and Both R. A. 1995. Trace elements in sulfide minerals from eastern Australian volcanic-hosted massive sulfide deposits; Part I, Proton-microprobe analyses of pyrite, chalcopyrite, and sphalerite, and Part II, selenium levels in pyrite; comparison with $\delta^{34}S$ values and implications for the source of sulfur in volcanogenic hydrothermal systems. *Economic Geology* 90:1167–1196.

Kerber L., Forget F., and Wordsworth R. 2015. Sulfur in the early Martian atmosphere revisited: Experiments with a 3-D global climate model. *Icarus* 261:133–148.

King P. L. and McLennan S. M. 2010. Sulfur on Mars. *Elements* 6:107–112.

Kiyosu Y. and Krouse R. H. 1990. The role of organic and acid in the in the sulfur abiogenic isotope reduction effect. *Geochemistry Journal* 24:21–27.

Koeberl C. 2014. The geochemistry and cosmochemistry of impacts. In *Planets, asteroids, comets and the solar system. Treatise on Geochemistry*, vol.2, 2nd ed, edited by Holland H. D. and Turekian K. K. Amsterdam: Elsevier. pp. 73–118.

Labidi J., Cartigny P., Birck J. L., Assayag N., and Bourrand J. J. 2012. Determination of multiple sulfur isotopes in glasses: A reappraisal of the MORB $\delta^{34}S$. *Chemical Geology* 334:189–198.

Labidi J., Farquhar J., Alexander C. M. O. D., Eldridge D. L., and Oduro H. 2017. Mass independent sulfur isotope signatures in CMs: Implications for sulfur chemistry in the early solar system. *Geochimica et Cosmochimica Acta* 196:326–350.

Leroux H., Jacob D., Marinova M., Hewins R. H., Zanda B., Pont S., Lorand J.-P., and Humayun M. 2016. Exsolution and shock microstructures of igneous pyroxene clasts in the NWA 7533 Martian meteorite. *Meteoritics & Planetary Sciences* 51:932–945.

Lindsay F. N., Turri B. D., Göpel C., Herzog G. F., Zanda B., Hewins R., Park J., Delaney J. S., and Swisher C. C. 2014. $^{40}Ar/^{39}Ar$ Ages of Martian meteorite NWA 7533 (abstract #5383). *Meteoritics & Planetary Sciences* 47.

Lorand J.-P., Alard O., Luguet A., and Keays R. R. 2003. S/Se systematics of the subcontinental lithospheric mantle beneath the Massif Central. *Geochimica et Cosmochimica Acta* 67:4137–4153.

Lorand J.-P., Barat J.-A., Chevrier V., Sautter V., and Pont S. 2012. Metal-saturated sulfide assemblages in chassignite NWA 2737: Evidence for impact-related sulfur devolatilisation. *Meteoritics & Planetary Science* 47:1830–1841.

Lorand J.-P., Chevrier V., and Sautter V. 2005. Sulfide mineralogy and redox conditions in some shergottites. *Meteoritics & Planetary Science* 40:1257–1272.

Lorand J.-P., Hewins R. H., Pont S., Zanda B., Humayun M., and Nemchin A. 2015. Nickeliferous pyrite tracks pervasive hydrothermal alteration in Martian regolith breccia: A study in NWA 7533. *Meteoritics & Planetary Sciences* 50:2099–2120.

Lorand J.-P., Pont S., Chevrier V., Luguet A., Zanda B., and Hewins R. H. 2018a. Petrogenesis of Martian sulfides in the Chassigny meteorite. *American Mineralogist* 103:872–885.

Lorand J.-P., Hewins R. H., Humayun M., Zanda B., Remusat L., La C., and Pont S. 2018b. Chalcophile-siderophile element systematics of hydrothermal pyrite from Martian regolith breccia NWA 7533. *Geochimica et Cosmochimica Acta* 241:134–149.

MacArthur J. C., Bridges L. J., Hicks Burgess R., Joy K. H., Branney M. J., Hansford G. M., Baker S. H., Schwenzer S. P., Gurman S. J., Stephen N. R., Steer E. D., Pierc J. D., and Ireland T. R. 2019. Mineralogical constraints on the thermal history of Martian regolith breccia Northwest Africa 8114. *Geochimica et Cosmochimica Acta* 246:267–298.

Machel H. G., Krouse H. R., and Sassen R. 1995. Products and distinguishing criteria of bacterial and thermochemical sulfate reduction. *Applied Geochemistry* 10:373–389.

Magnall J. M., Gleeson S. A., Stern R. A., Newton R. J., Poulton S. W., and Paradis S. 2016. Open system sulfate reduction in a diagenetic environment—Isotopic analysis of barite ($\delta^{34}S$ and $\delta^{18}O$) and pyrite ($\delta^{34}S$) from the Tom and Jason Late Devonian Zn–Pb–Ba deposits, Selwyn Basin, Canada. *Geochimica et Cosmochimica Acta* 180:146–163.

Mari N., Riches A. J. V., Hallis L. J., Marrocchi Y., Villeneuve J., Gleissner P., Becker H., and Lee M. 2019. Syneruptive incorporation of Martian surface sulphur in the nakhlite lava flows revealed by S and Os isotopes and highly siderophile elements: Implication for mantle sources in Mars. *Geochimica et Cosmochimica Acta* 266:416–43.

Masterson A. L., Farquhar J., and Wing B. A. 2011. Sulfur mass-independent fractionation patterns in the broadband UV photolysis of sulfur dioxide: Pressure and third body effects. *Earth & Planetary Science letters* 306:253–260.

McCubbin F. M., Tosca N. J., Smirnov A., Nekvasil H., Steele A., Fries M., and Lindsley D. H. 2009. Hydrothermal jarosite and hematite in a pyroxene-hosted melt inclusion in Martian meteorite Miller Range (MIL) 03346: Implications for magmatic-hydrothermal fluids on Mars. *Geochimica et Cosmochimica Acta* 73:4907–4917.

McCubbin F. M., Boyce J. W., Nováʹk-Szaboʹ T., Santos A. R., Tartese R., Muttik N., Domokos G., Vazquez J., Keller L. P., Moser D. E., Jerolmack D. J., Shearer C. K., Steele A., Elardo S. M., Rahman Z., Anand M., Delhaye T., and Agee C. B. 2016. Geologic history of Martian regolith breccia Northwest Africa 7034: Evidence for hydrothermal activity and lithologic diversity in the Martian crust. *Journal of Geophysical Research* 121:2120–2149.

McLennan S. M., Bell J. F., Calvin M., Christensen P. R., Clark B. C., De Souza P. A., Farmer J., Farrand W. H., Fike D. A., Gellert R., Ghosh A., Glotch T. D., Grotzinger J. P., Hahn B., Herkenhoff K. E., Huorwitz J. A., Johnson J. R., and Yen A. 2005. Provenance and diagenesis of the evaporite-bearing Burns formation, Meridiani Planum, Mars. *Earth & Planetary Science Letters* 240:95–121.

Moser D. E., Arcuri G.A., Reinhard D. A., White L. F., Darling J. R., Barker I. R., Larson D. J., Irving A. J., McCubbin F. M., Tait K. T., Roszjar J., Wittmann A., and Davis C. 2019. Decline of giant impacts on Mars by

4.48 billion years ago and an opportunity for early habitability. *Nature Geoscience* 12:522–527.

Muller E., Philippot P., Rollion-Bard C., and Cartigny P. 2016. Multiple sulfur-isotope signatures in Archean sulfates and their implications for the chemistry and dynamics of the early atmosphere. *Proceedings of the National Academy of Sciences of the United States of America* 113:7432–7437.

Muller E., Philippot P., Rollion-Bard C., Cartigny P., Assayag N., Marin-Carbonne J., and Sarma D. S. 2017. Primary sulfur isotope signatures preserved in high-grade Archean barite deposits of the Sargur Group, Dharwar Craton, India. *Precambrian Research* 295:38–47.

Nachon M., Clegg S. M., Mangold N., Schroder S., Kah L. C., Dromart G., Ollila A., Johnson J. R., Oehler D. Z., Bridges J. C., Le Mouelic S., Forni O., Wiens R. C., Anderson R. B., Blaney D. L., Bell J. F. I., Clark B., Cousin A., Dyar M. D., Ehlmann B., Fabre C., Gasnault O., Grotzinger J., Lasue J., Lewin E., Leveille R., McLennan S., Maurice S., Meslin P. Y., Rapin W., Rice M., Squyres S. W., Stack K., Sumner D. Y., Vaniman D., and Wellington D. 2014. Calcium sulfate veins characterized by ChemCam/Curiosity at Gale crater, Mars. *Journal of Geophysical Research Planets* 119:1991–2016.

Naumov M. 2005. Principal features of impact-generated hydrothermal circulation systems: Mineralogical and geochemical evidence. *Geofluids* 5:165–180.

Newsom H. E. 1980. Hydrothermal alteration of impact melt sheets with implications for Mars. *Icarus* 44:207–216.

Nyquist L. E., Bogard D. D., Shii C. Y., Greshake A., Stöffler D., and Eugster O. 2001. Ages and geological histories of Martian meteorites. *Space Science Reviews* 96:105–164.

Ohno S., Wing B., Rumble D., and Farquhar J. 2006. High precision analysis of all four stable isotopes of sulfur (^{32}S, ^{33}S, ^{34}S and ^{36}S) at nanomole levels using a laser fluorination isotope-ratio-monitoring gas chromatography-mass spectrometry. *Chemical Geology* 225:30–39.

Osinski G. R., Tornabene L. T., Banerjee N. R., Cockell C. S., Flemming R., Izawa M. R., McCutcheon J., Parnell J., Preston L. J., Pickersgill A. E., Pontefract A., Sapers H., and Southam G. 2013. Impact-generated hydrothermal systems on Earth and Mars. *Icarus* 347–363.

Parat F., Holtz F., and Streck M. 2011. Sulfur-bearing magmatic accessory minerals. *Review Mineralogy and Geochemistry* 73:285–314.

Parnell J., Taylor W. C., Thackrey S., Osinski G. R., and Lee P. 2010. Permeability data for impact breccias imply focused hydrothermal fluid flow. *Journal of Geochemical Exploration* 106:171–175.

Pavlov A. A. and Kasting J. F. 2002. Mass-independent fractionation of sulfur isotopes in Archean sediments: Strong evidence for an anoxic Archean atmosphere. *Astrobiology* 2:27–41.

Peslier A. H., Hervig R., Yang S., Humayun M., Barnes J. J., Irving A. J., and Brandon A. D. 2019. Determination of the water content and D/H ratio of the Martian mantle by unravelling degassing and crystallization effects in nakhlites. *Geochimica et Cosmochimica Acta* 266:382–415.

Philippot P., Van Zuilen M., and Rollion-Bard C. 2012. Variations in atmospheric sulfur chemistry on early Earth linked to volcanic activity. *Nature Geoscience* 5:668–674.

Pierazzo E. and Artemieva N. 2012. Local and global environmental effects of impacts on earth. *Elements* 8:55–60.

Righter K., Pando K., and Danielson L. R. 2009. Experimental evidence for sulfur-rich Martian magmas: Implications for volcanism and surficial sulfur sources. *Earth & Planetary Science Letters* 288:235–243.

Righter K., Abell P., Agresti D., Berger E. L., Burton A. S., Delaney J. S., Fries M. D., Gibson E. K., Haba M. K., Harrington A., Herzog G. F., Keller L. P., Locke D., Lindsay F. N., McCoy T. J., Morris R. V., Nagao K., Nakamura-Messenger K., Niles P. B., Nyquist L. E., Park J., Peng Z. X. F., Shii C. Y., Simon J. I., Swisher C. C., Tappa M. J., Turrin B. D., and Zeigler R. A. 2015. Mineralogy, petrology, chronology, and exposure history of the Chelyabinsk meteorite and parent body. *Meteoritics & Planetary Science* 50:1790–1819.

Schwenzer S. P. and Kring D. A. 2013. Alteration minerals in impact-generated hydrous alteration systems—Exploring host rock variability. *Icarus* 226:487–496.

Seal R. 2006. Sulfur isotope geochemistry of sulfide minerals. *Review in Mineralogy and Geochemistry* 61:633–677.

Shanks W. C. III. 2014. Stable isotope geochemistry of mineral deposits. In *reatise on geochemistry* edited by Holland H. D. and Turekian K. K. Amsterdam: Elsevier. pp. 59–85. doi: 10.1016/B978-0-08-095975-7.01103-7

Shearer C. K., Layne G. D., Papike J. J., and Spilde M. N. 1996. Sulfur isotopic systematics in alteration assemblages in Martian meteorite Allan Hills 84001. *Geochimica et Cosmochimica Acta* 60:2921–2926.

Simpson S. L., Osinski G. R., Lee P., Parnell J., Spray J. G., and Baron M. 2005. A case study of impact-induced hydrothermal activity: The Haughton impact structure, Devon Island, Canadian High Arctic. *Meteoritics & Planetary Science* 40:1859–1877.

Simpson S. L., Boyce A. J., Lambert P., Lindgren P., and Lee M. R. 2017. Evidence for an impact-induced biosphere from the δ^{34}S signature of sulfides in the Rochechouart impact structure, France. *Earth & Planetary Science Letters* 460:192–200.

Squyres S. W., Arvidson R. E., Bell J. F., Calef F., Clark B. C., Cohen B. A., Crumpler L. A., de Souza P. A., Farrand W. H., Gellert R., Grant J., Herkenhoff K. E., Hurowitz J. A., Johnson J. R., Jolliff B. L., Knoll A. H., Li R., McLennan S. M., Ming D. W., Mittlefehldt D. W., Parker T. J., Paulsen G., Rice M. S., Ruff S. W., Schröder C., Yen A. S., and Zacny K. 2012. Ancient impact and aqueous processes at Endeavour crater, Mars. *Science* 336:570–576.

Thomassot E., Cartigny P., Harris J., Lorand J.-P., Rollion-Bard C., and Chaussidon M. 2009. Metasomatic diamond growth: A multi-isotope study (^{13}C, ^{15}N, ^{33}S, ^{34}S) of sulfide inclusions and their host diamonds from Jwaneng (Botswana). *Earth & Planetary Science Letters* 282:79–90.

Tian F., Mark W., Claire B., Jacob D., Haqq M., Smith M., Crisp D. C., Catling D., Zahnle K., and Kasting J. F. 2010. Photochemical and climate consequences of sulfur outgassing on early Mars. *Earth & Planetary Science Letters* 295:412–418.

Wang Z. and Becker H. 2017. Chalcophile elements in Martian meteorites indicate low sulfur content in the Martian interior and a volatile element-depleted late veneer. *Earth and Planetary Science Letters* 463:56–68.

Wentworth S. J. and Gooding J. L. 1994. Carbonates and sulfates in the Chassigny meteorite: Further evidence for aqueous chemistry on the SNC parent planet. *Meteoritics & Planetary Science* 29:860–863.

Whitehouse M. J. 2013. Multiple sulfur isotope determination by SIMS: Evaluation of reference sulfides for Δ^{33}S with observations and a case study on the determination of Δ^{36}S. *Geostandard & Geoanalytical Research* 37:19–33.

Wu N., Farquhar J., Strauss H., Kim S., and Canfield D. 2010. Evaluating the S-isotope fractionation associated with Phanerozoic pyrite burial. *Geochimica et Cosmochimica Acta* 74:2050–2071.

Young E.D., Galy A., Nagahara H. 2002. Kinetic and equilibrium mass-dependent isotope fractionation laws in nature and their geochemical and cosmochemical significance. *Geochimica Cosmochimica Acta* 66 :1095-1104.

Ziemkiewicz P. F., O'Neal M., and Lovett R. J. 2011. Selenium leaching kinetics and in situ control. *Mineral Water Environment* 30:141–150.

Zolotov M. Y. and Shock E. L. 2005. Formation of jarosite-bearing deposits through aqueous oxidation of pyrite at Meridiani Planum, Mars. *Geophysical Research Letters* 32: L21203.